electronics

MDPI

Review

Power Converters for Green Hydrogen: State of the Art and Perspectives

Gianpaolo Vitale

Consiglio Nazionale delle Ricerche, ICAR, Institute for High Performance Computing and Networking, National Research Council of Italy, 90146 Palermo, Italy; gianpaolo.vitale@icar.cnr.it

Abstract: This paper provides a comprehensive review and outlook on power converters devised for supplying polymer electrolyte membrane (PEM) electrolyzers from photovoltaic sources. The produced hydrogen, known as green hydrogen, is a promising solution to mitigate the dependence on fossil fuels. The main topologies of power conversion systems are discussed and classified; a loss analysis emphasizes the issues concerning the electrolyzer supply. The attention is focused on power converters of rated power up to a tenth of a kW, since it is a promising field for a short-term solution implementing green hydrogen production as a decentralized. It is also encouraged by the proliferation of relatively cheap photovoltaic low-power plants. The main converters proposed by the literature in the last few years and realized for practical applications are analyzed, highlighting their key characteristics and focusing on the parameters useful for designers. Future perspectives are addressed concerning the availability of new wide-bandgap devices and hard-to-abate sectors with reference to the whole conversion chain.

Keywords: green hydrogen; water electrolysis; clean energy; photovoltaic generation; DC/DC converter

Citation: Vitale, G. Power Converters for Green Hydrogen: State of the Art and Perspectives. *Electronics* **2024**, *13*, x. https://doi.org/10.3390/xxxxx

Academic Editor: Pedro J. Villegas

Received: 16 September 2024
Revised: 14 November 2024
Accepted: 15 November 2024
Published: date

1. Introduction

Hydrogen is widely recognized as a zero-carbon energy carrier and can play a crucial role in addressing issues related to climate change [1]. It is a promising solution for storing energy and produces zero-emission, as fuel burned with oxygen [2,3]. As a consequence, hydrogen roadmaps have been conceived and applied by an increasing number of countries [4]. Paper [5] recognizes, as a relevant element of carbon-neutral Power-2-X applications, the combination of hydrogen generated from renewable electricity and CO_2 captured from the atmosphere. The urgency of immediate actions to reduce greenhouse gas emissions and lower the Earth's temperature has led the European Union (EU) to the ambitious goals of reducing emissions by at least 55% by 2030, compared to the 1990 levels, and to become the first climate-neutral continent by 2050 [6].

Hydrogen can be produced by different methods. At the moment, fossil energy reforming is the most popular solution; it has the lowest cost but implies the generation of a significant amount of carbon dioxide [7]. On the other hand, there is a broad selection of methods used to obtain hydrogen sustainably; they encompass fossil energy reforming, industrial by-product gas, water electrolysis (WE), and other technologies still in the experimental stage [8–10].

Water electrolysis produces no carbon emissions. Currently, it exhibits a higher cost than other methods [11]; however, it is more attractive when supplied by renewable energy sources (RESs), such as wind and photovoltaic energy, since the process displays a fluctuating power [12,13]. Recent studies (2020–2023) do not believe water electrolysis holds economic promise within the next few years [14]. However, the situation is expected to change in the medium term, when the expected cost will be lower than 2.5 $/kg

H_2 by 2030 [15] and will be further reduced to 2.5 \$/kg H_2 by 2050 [16]. Consequently, this solution is expected to become cost-effective compared to other methods [17]. In aid of this prediction, oxygen (O_2) generated as a by-product is considered a source of income.

There are different technologies for water electrolysis in the market, for instance, Alkaline electrolysis is available up to a MW scale [17,18]; Polymer Electrolyte Membrane (PEM) electrolyzers (EL) are attractive when the power supply is delivered by renewable energies [19,20]; and solid oxide (SO) electrolyzers exhibit a higher efficiency, though their low lifetime and high fabrication costs do not currently make them feasible for industrial use [21].

Polymer Electrolyte Membrane electrolyzers (PEM-ELs) are expected to replace alkaline systems; they could become the most common solution for hydrogen generation in 2030 [19]. At the moment, an obstacle is represented by the cost of metal materials employed; however, once the operational cost is lessened, PEM electrolyzers may also be extended to industrial applications [20]. Among the advantages of PEM electrolyzers are the reduced operational cost, high current density (above 2 A/cm^2), and low ohmic drops thanks to a thinner electrolyte compared to the alkaline EL. In addition, the PEM-EL operates in a wide range of power inputs for the fast response of the proton transport across the membrane. For these reasons, they are particularly suitable to be powered by photovoltaic sources [7,22]; it is expected that they will encourage the research and design of new converters [23–26]. On the other hand, the PEM-EL lifetime is still lower than that of alkaline systems under fluctuating operating conditions [27]. For these reasons, this paper mainly focuses on DC/DC converters devised for the PEM-EL supply; it discusses the main issues regarding design and performance, which are different from applications of the same converters in different fields because of the constraints imposed by the electrolyzers. Converters with powers up to ten kW are analyzed because there is great potential in this field for distributed generation, even in domestic applications [14,17].

Although hydrogen is inherently a nonpolluting energy carrier, the energy source from which it is produced must be considered in terms of its pollutant emissions. For this reason, hydrogen is associated with a corresponding color. At the moment, the most common method for hydrogen production, which shows mature technology use and a low production cost, is based on the conversion reaction of fossil fuels. If carbon emissions are generated during the process, it is called gray hydrogen [28,29]. Carbon emissions can be processed by technologies such as carbon capture and carbon sequestration (CCUS) to produce blue hydrogen. Finally, water electrolysis by renewable sources gives green hydrogen; in this case, almost no greenhouse gas is derived during the production process [30].

It is evident that to manage an environmental-friendly vector of energy, all efforts should tend toward green hydrogen production; however, there are still technical thresholds and a high cost to be faced before achieving large-scale production [12,31–34].

For the above-mentioned reasons, in the hydrogen production framework, this paper considers the power converters supplied by photovoltaic sources for producing green hydrogen exploiting water electrolysis by PEM-ELs. A graphical representation of this planning is shown in Figure 1. The PEM-based electrolysis is a subset of water electrolysis that falls under the field of green hydrogen generation. In this field, converters are being researched both in terms of new topologies and with traditional circuits that must be considered based on the constraints imposed by the electrolyzer. The electrolyzer requires a DC voltage generally lower than that of the source, high currents, minimal voltage ripple, and the absence of overvoltages in dynamic behavior.

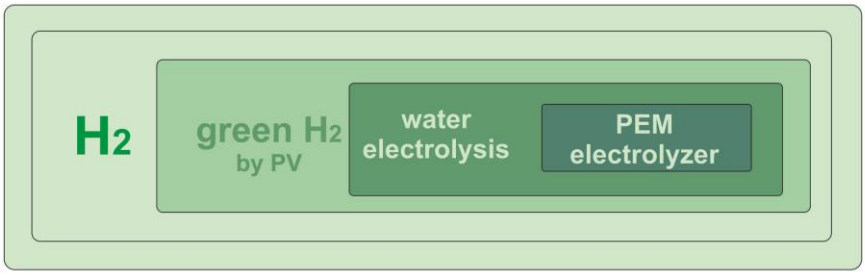

Figure 1. Graphical overview of the approach proposed by this paper; in the context of hydrogen production, we consider that produced from photovoltaic sources by the electrolysis of water with PEM-type electrolyzers.

This approach makes this review different from others recently published in the literature; in fact, [9] is focused on hydrogen production processes as well as [20,29]. Papers [23,24] deal with PEM water electrolysis, whereas [35] considers PEM electrolyzers supplied by renewables, introducing the need for a converter system to be used as a power interface, even if the topologies are not addressed. Some surveys consider specific applications such as grid services [36] and the use of hydrogen as a storage system [37]. High-power converter applications for large-scale hydrogen production via water electrolysis are described in [38,39], concerning the use of IGBT or thyristors. Paper [40] mainly focuses on the architecture, including electrolyzer modeling; paper [41] deals with DC/DC converters, and it evidences some challenges, such as output ripple reduction, efficiency optimization, cost minimization, and robustness against failures. Papers [42,43] are dedicated to the interleaved converters. Paper [27] gives a complete overview of the integration of water electrolyzers and photovoltaic (PV) solar technology; however, it does not deal with power conversion circuits. A review of power converters is given in [10,31,44]; the structure of this paper is similar to that of these last three papers. In addition, it discusses the presented converters, taking into consideration the main constraints in terms of efficiency, ripple, and cost. It is up to date compared to [10,44], since references encompass seven papers published in the first half of 2024. Compared to [31], the proposed work is more design-oriented since it includes a deep analysis of DC/DC converters specifically devised for PEM electrolyzers. After the introduction, a losses overview focused on PEM electrolyzers is given, and the ways in which a suitable choice of parameters can optimize efficiency are discussed. The power converters are classified into non-isolated and isolated, and the constraints imposed by the high-output currents are discussed in the analysis proposed in the following sections. Finally, the perspectives opened by new power devices such as SiC and GaN and some hard-to-abate sectors concerning the whole conversion chain are addressed.

2. PEM Electrolysis

PEM electrolysis cells offer several advantages, for instance, there is a high current density (above 2 A/cm^2), the operational cost is reasonable, and ohmic voltage drops are reduced compared to the alkaline electrolyzer since the electrolyte is thinner [7]. Moreover, the PEM electrolyzer exhibits a fast response of the proton transport across the membrane, resulting in suitable operation with a wide range of power inputs, as the power is delivered by renewable energy sources whose delivered energy is affected by abrupt variations [12,13]. Finally, the PEM electrolyzer produces high-pressure hydrogen, performing an electrochemical compression; this feature makes storage easier.

The chemical reaction carried out to obtain hydrogen is described by Equation (1), which considers the Gibbs energy (237 kJ·mol^{-1}) and the lost energy (48.6 kJ·mol^{-1}). Gibbs energy is the minimum work necessary for the reaction to proceed, whereas lost energy is converted into heat due to losses in the anode and in the cathode.

$$H_2O + 237.2\left[\frac{kJ}{mol_{(Gibbs)}}\right] + 48.6\left[\frac{kJ}{mol_{(heat)}}\right] \rightarrow H_2 + \frac{1}{2}O_2 \quad (1)$$

Starting from the water molecule, protons and oxygen are obtained providing electrons according to the following sub-reaction:

$$H_2O \rightarrow 2H^+ + \frac{1}{2}O_2 + 2e^- \quad (2)$$

The available electrons flow through the anode, resulting in a current flowing into the anode, and the protons flow through the membrane. Once the protons reach the cathode, they combine with electrons originating from the terminal at the negative potential and obtain hydrogen as follows:

$$2H^+ + 2e^- \rightarrow H_2 \quad (3)$$

Figure 2 schematically shows the operation; the anode is connected to a positive electric potential, and a current is imposed on the electrolyzer to guarantee the electrons' flow.

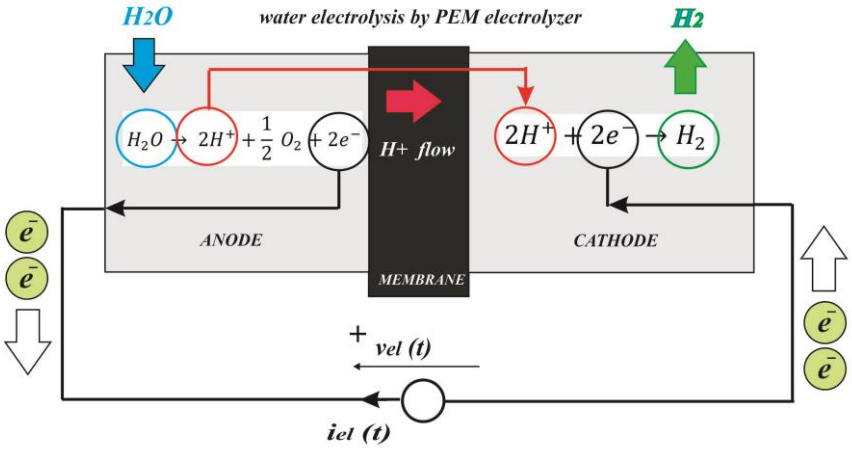

Figure 2. Diagram of PEM water electrolysis reactions.

From this analysis, it can be deduced that the electrolyzer is a current-driven device. The volume of hydrogen is proportional to the current density [45].

Unfortunately, the power supplied to the PEM electrolyzer cannot be completely converted into high-pressure hydrogen because of the losses. A simplified physical model that can be used to reproduce the hydrogen production and losses is depicted in Figure 3. Particularly, the Gibbs energy, the membrane and losses into the two sub-reactions, and the produced hydrogen are modeled by a series connection of resistance and a counter-electromotive force generator, respectively. More complicated models can also reproduce dynamic behavior; they adopt a parallel connection of an equivalent resistance and a capacitance for the anode and cathode [22]. These models are required to suitably reproduce dynamic transients.

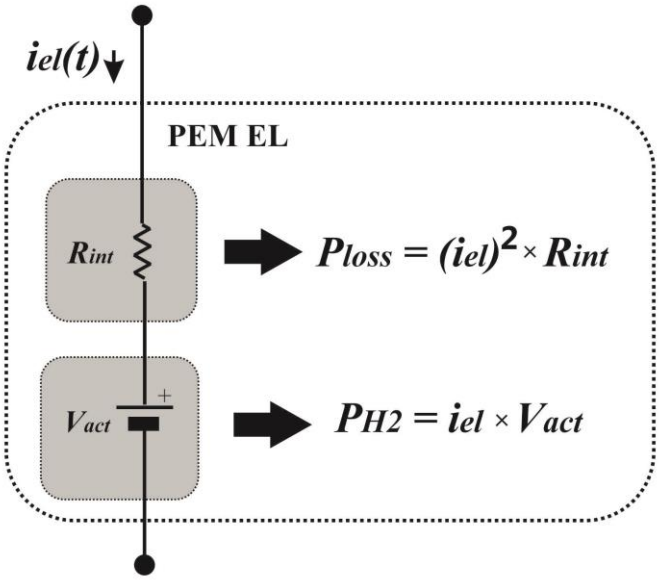

Figure 3. Simplified static linear model of a PEM-EL showing the breakdown of the power supplied by the generator partly converted to hydrogen and partly lost as heat.

The counter-electromotive voltage value corresponds to the reversible voltage, representing the minimum needed energy barrier of the electrolyzer; the hydrogen production starts when the voltage applied to the electroyzer is greater than V_{act}. The current versus voltage characteristic starts with this value at zero current and then shows a non-linear increasing trend with the current. Adopting the resistance and a voltage generator, the model is approximated by a linear voltage vs. current characteristic. The power corresponding to the current flowing through the counter-electromotive force generator is effectively converted into hydrogen, whereas the current flowing through the resistance generator corresponds to the power lost. A higher current increases hydrogen production but worsens the PEM efficiency since the amount of hydrogen is proportional to the current, while the losses increase with the square of the current. Based on the supplied current I_{el}, in stationary conditions, the volume of hydrogen V_{H2} can be calculated by the following equation based on the Faraday law [46]:

$$V_{H2} = \frac{R \cdot I_{el} \cdot \Delta t \cdot T}{F \cdot p \cdot z} \quad (4)$$

where R is the ideal gas constant (equal to 8.3145 J/mol K), T is the temperature in [K], Δt is the time interval the current is supplied, F is the Faraday's constant (equal to 9.64×10^4 C/mol), p is the ambient pressure, and z is the number of excess electrons (equal to 2 for hydrogen).

At a constant temperature, the conductivity of the PEM electrolyzer decreases non-linearly with the pressure, whereas with constant pressure, the conductivity increases linearly with temperature. The conductivity variation requires a constant current to be supplied to produce a constant hydrogen volume with the expected efficiency [47,48]. Finally, a constant current supply allows the removal of a defective cell (hot-swap) without stopping the operation.

Although most converters analyzed are voltage generators, a converter's control algorithm can be entrusted with the task of maintaining a constant current. The algorithm adjusts the output voltage based on the amount of hydrogen to be produced, and thus, the current to be supplied.

Water Electrolysis by PEM Electrolyzers Supplied by Photovoltaic Sources

When a photovoltaic source is exploited to supply a PEM electrolyzer, the power converter has the task of tracking the maximum power point on the PV source, characterized by a couple of voltage and current values (V_{mpp}, I_{mpp}), varying the solar radiation, and transferring the delivered power to the electrolyzer. The conversion chain is illustrated in Figure 4, where the source is connected to the DC/DC converter; its voltage output is applied to the electrolyzer.

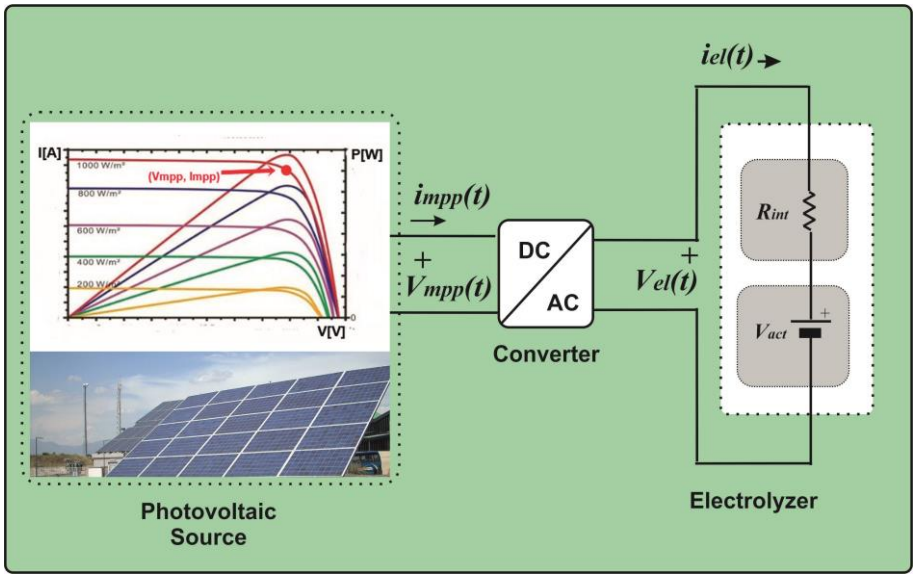

Figure 4. Structure of a conversion chain supplied by a photovoltaic source.

The related power balance, neglecting the losses on the converter is given by:

$$V_{mpp} \cdot I_{mpp} = I_{el}^2 \cdot R_{int} + I_{el} \cdot V_{act} \quad (5)$$

where according to Figure 4, I_{el} is the current flowing through the electrolyzer, R_{int} is the internal resistance, and V_{act} is the activation voltage. The power converter must apply a voltage to the electrolyzer so that the related current satisfies Equation (5). This current depends on the electrolyzer's equation, which is as follows:

$$I_{el} = \frac{V_{el} - V_{act}}{R_{int}} \quad (6)$$

By substituting Equation (6) into Equation (5), a second-order equation is obtained, whose positive solution represents the converter's output voltage to be applied to the electrolyzer.

$$V_{el}^2 - V_{el} \cdot V_{act} - \left(V_{mpp} \cdot I_{mpp}\right) \cdot R_{int} = 0 \quad (7)$$

The DC/DC power conversion systems are driving research, especially for medium-low power levels [10]. These converters can be either in a transformerless or in isolated configuration (as described below, a high-frequency intermediate transformer can be used to improve the step-down ratio and achieve other benefits such as the galvanic isolation between the source and the load). Such systems are taken into consideration as equipped with supplementary storage elements, or more generally to support DC microgrids as well [49].

Although the converters that can be used are mostly known, their use in the field of electrolyzers poses different specifications that come from the source and the load, affecting the topology and the design of the converter. Concerning the constraints imposed by the electrolyzer, first of all, the DC voltage produced by the PV plant is usually much higher than that required by the electrolyzer, imposing a high step-down ratio [23,24].

Secondly, the delivered power depends on solar radiation. Hence, the supplied DC voltage changes over time and can also be subjected to abrupt variations in partial or total shading; it requires tracking the maximum available power by the DC/DC converter. If the power produced by the PV plant is lower than the rated power of the electrolyzer, the delivered hydrogen is consequently diminished. The PEM electrolyzer needs a DC voltage with minimum ripple to preserve the membrane [50]; the supply voltage must not exceed the maximum prescribed value, which means that the dynamic behavior during the transients must avoid voltage overshoots. The requirement of minimum voltage ripple also implies a suitable design of EMI filters, if required, since they affect the control behavior [51]. The dynamic behavior of the power converter is affected by the dynamic behavior of the electrolyzer, which should be considered in the converter design [52]. As a consequence, the converter topology is selected to optimize the energy transfer under steady-state conditions; then, the control system is designed to retrieve the best matching during transients.

Finally, the converter's efficiency plays a crucial role as it allows generated power to be converted into hydrogen as much as possible. A higher efficiency reduces both the design and production costs because the heat dissipation equipment is cheaper and so is the operating cost. After all, it increases the amount of hydrogen per given power, lowering the payback time [14,17]. Because of the relevant role of efficiency, the next section describes the main causes of losses in power converters and ways to optimize them.

3. Losses Analysis in Power Converters

The power converter's efficiency plays a crucial role; the target is to achieve the lowest losses, making the efficiency as close to the unit value and forming a flat curve as the converter power varies. Unfortunately, the losses vary depending on the current flowing through the various devices.

Efficiency is defined by the ratio of the output power (P_o) over the input power (P_i); they differ because of the power lost in the converter (P_{diss}).

$$\eta = \frac{P_o}{P_i} = \frac{P_o}{P_o + P_{diss}} = \frac{1}{1 + \frac{P_{diss}}{P_o}} \approx 1 - \frac{P_{diss}}{P_o} \tag{8}$$

The losses can be classified as (a) constant losses (auxiliary cooling devices, capacitive switching losses), (b) losses linearly dependent on the current (as in semiconductors junctions with constant forward voltage drop), (c) losses quadratic with the current (as in semiconductors characterized by a conduction resistance) or Joule losses.

$$P_{diss} = k_o + k_l P_o + k_q P_o^2 \tag{9}$$

Maximum efficiency is achieved when constant and quadratic losses are equal; a demonstration is given in Appendix A. Since Equation (9) represents a parabolic curve, the efficiency curve shows a maximum that usually does not coincide with the rated power of the converter; it means that the efficiency is worsened in proximity to the rated power [53]. Since an electrolyzer needs high currents at the rated power, the efficiency decrease represents an issue; some converters are conceived to retrieve a flat efficiency curve.

A detailed loss analysis allows for the recognition of the main losses and how they can be managed in the case of electrolyzer supply.

The losses in a power converter can be classified as shown in Figure 5. They are grouped into static and non-static (dynamic) losses. Concerning static losses, conduction losses often play a key role; on the contrary, blocking losses are not relevant due to the negligible leakage currents. Dynamic losses occur during commutation due to the simultaneous presence of both voltage and current at the power device's terminals; they can be classified as turn-on, turn-off, and reverse recovery losses. A great deal of effort by designers is therefore directed toward solutions avoiding the simultaneous presence of

current and voltage at the device terminals, as will be shown in the following sections. Finally, driving losses depend both on the driving circuit and the gate capacitance charged and discharged at each commutation [54].

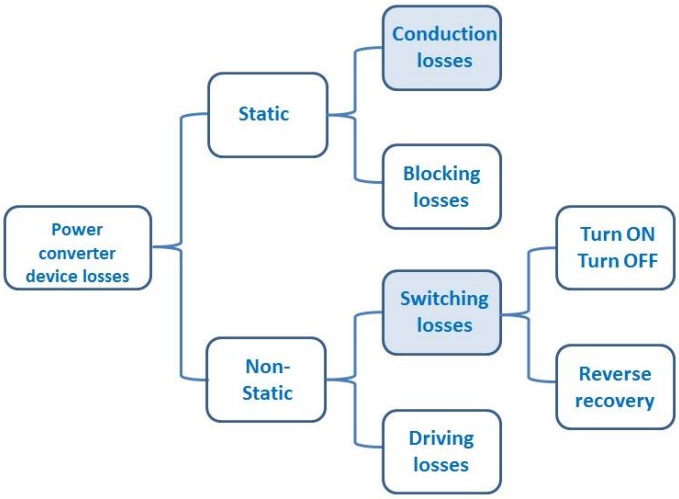

Figure 5. Losses classification.

The general expression of the mean power lost for a power device subjected to a voltage $v(t)$, in which flows a current $i(t)$ in a time t_1, calculated in a switching period T, is given as follows:

$$P_{loss} = \frac{1}{T}\int_0^{t_1} i(t)\, v(t)\, dt \tag{10}$$

Concerning the conduction losses, the integration time is the conduction time t_{on}. Equation (10) can be particularized for devices that show either a constant voltage drop v_{CE} (as IGBTs) or a conduction resistance R_{ON} during conduction (as MOSFETs).

$$P_{cond\_IGBT} = \frac{1}{T}\int_0^{t_{on}} i(t)\, v_{CE}\, dt \tag{11}$$

$$P_{cond\_MOSFET} = \frac{1}{T}\int_0^{t_{on}} i^2(t)\, R_{ON}\, dt \tag{12}$$

Equation (11) can also be used to calculate the conduction losses in a diode by changing v_{CE} with the drop voltage across the diode V_γ. The switching losses depend on the contemporary presence of both voltage and current during commutation; under the assumption of a triangular-shaped instantaneous power, the power lost in an on–off–on commutation is given as follows:

$$P_{sw} = \frac{1}{2} VI(t_{turn\_on} + t_{turn\_off}) f_s \tag{13}$$

where V and I are the voltage in the blocking state and the conduction current, respectively; t_{turn_on} is the time required to turn on the device, which encompasses the fall time tf (time interval in which the voltage drops to zero) and the rise time tr (time necessary for the current to rise from zero to its final value). Similarly, t_{turn_off} is the time required to turn off the device; it encompasses the time interval in which the current falls to zero and the time to increase the voltage up to the blocking value, and f_s is the switching frequency. Designers make great efforts to minimize the voltage or current during switching, aiming for zero-voltage switching (ZVS) or zero-current switching (ZCS). The reverse recovery losses occur in a diode when it switches from the conducting to the blocking state; the current falls to null value and remains negative (reverse recovery current) for a time in-

terval t_{rr} (reverse recovery time). The presence of a negative voltage during this time causes dissipation.

$$P_{rr} = \frac{1}{6} t_{on} V_{DD} I_{RRM} f_s \tag{14}$$

where V_{DD} is the diode blocking voltage, I_{RRM} is the maximum reverse recovery current, which is specified in the diode datasheet. This parameter increases significantly with temperature, the current derivative, and the current [55].

Parasitic elements also contribute to losses. The parasitic resistance of power inductors r_{paras} is often affected by a continuous (DC) component of the current and a periodic (AC) component; the related Joule losses are given as follows:

$$P_{Joule\_ind} = \frac{1}{T_s} \int_0^{T_s} (i_{DC}^2 + i_{AC}^2)\ r_{paras}\, dt \tag{15}$$

Filter capacitors are subjected to Joule losses because of their parasitic resistance r_{esr}; however, they are only affected by the AC component. Moreover, structural failures in electrolytic capacitors are often due to power dissipation inside the component, worsening the reliability of the whole conversion system [56,57].

$$P_{Joule\_cap} = \frac{1}{T_s} \int_0^{T_s} (i_{AC}^2)\ r_{esr}\, dt \tag{16}$$

Other losses from parasitic elements concern stray inductors and capacitors that originate from the layout and connection wires; they are charged/discharged with each switching period. As an example, a stray inductance L in a series with a power switch (due to its connections, including the connection inside its packaging) generates power dissipation as follows:

$$P_{sw\_L} = \frac{1}{2} L\, i^2\, f_s \tag{17}$$

Another effect to be accounted for, given by stray inductances, consists of voltage overshoots originating from the high current commutation of fast switching devices. In fact, by the constitutive inductor Equation (18), it can be deduced that across the stray inductance, due to a high current variation in a short time, a voltage spike can occur since, with turn-on or turn-off times of tenths on the order of nanoseconds, a stray inductance of a tenth of a nanohenry and a current variation in tenths of an ampere can generate a relevant voltage pulse.

$$v_L = L\left(\frac{di_L}{dt}\right) \tag{18}$$

Similarly, a stray capacitance C in parallel on a switch causes power dissipation corresponding to the transferring of the capacitance energy to the switch at its turn-on.

$$P_{sw\_C} = \frac{1}{2} C\, v^2\, f_s \tag{19}$$

Both losses described by Equations (17) and (19) are proportional to the switching frequency. The same considerations hold for the gate capacitance of MOSFET-based power switches, unless more sophisticated driving techniques are adopted; in this case, a part of the energy is recovered [58].

Losses are recognized in magnetic materials adopted for inductors and transformers. In a soft magnetic material, the losses due to an applied variable magnetic field can be separated into three main contributions, the hysteresis, the eddy current, and the excess losses [59–61]. The hysteresis losses are due to the steady state losses of the Weiss domain; they are given as follows:

$$P_{mag\_H} = a\, f_s B^x m M \tag{20}$$

where B is the peak value of the flux density, f_s is the frequency, a is a coefficient dependent on the material, x is the Steinmetz coefficient, m is the number of toroids used for the magnetic core, and M is its weight in kg.

The eddy current losses are due to the presence of eddy current in the material, and they are given as follows:

$$P_{ec} = b f_s^2 (B)^2 mM \quad (21)$$

where b is a coefficient dependent on the magnetic material.

Finally, the excess losses due to the dynamic losses of the Weiss domain are obtained as follows:

$$P_{ex} = e f_s^{3/2} (B)^{3/2} mM \quad (22)$$

where e is a coefficient dependent on the magnetic material.

Usually, the coefficients are known for their sinusoidal waveforms; they are unsuitable in power converters where inductors are subjected to periodical, but non-sinusoidal solicitations, and more sophisticated models are required. The revised generalized Steinmetz model has retrieved the use of an equivalent resistance to model the core losses under triangular excitation [62,63].

In Equations (20)–(22), the dependence on frequency can be recognized. From this perspective, by increasing the switching frequency, the temperature of the inductor rises too. It may require attention when it is operated at the boundary of the linear zone since, in general, outside this zone, the increase in the temperature makes the inductance lower, leading, in some cases, to instability [64]. An analysis example of the main losses in a practical case is given in Appendix B.

Several parameters can contribute to optimizing efficiency. Two different steps concerning the converter design and control measures can be recognized as shown in Figure 6.

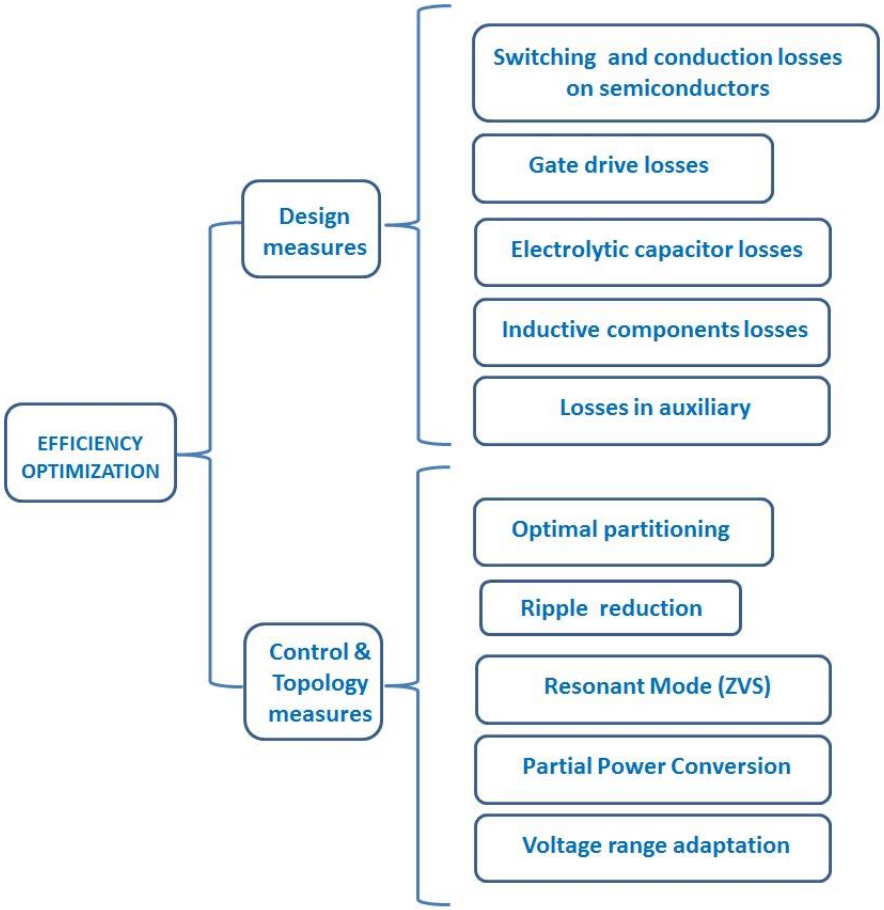

Figure 6. Outlook on optimization solutions.

3.1. Design Measures

The power switches make a considerable contribution to the converter losses; they are subjected to both switching and conduction losses. The designer has to minimize this contribution by making a suitable choice of power switches. Concerning dynamic losses, a lower turn-on and turn-off time allows diminishing switching losses according to Equation (13). Reverse recovery in power diodes is reduced by a suitable choice of device and imposing commutation with zero current; this feature is pivotal for the electrolyzer supply since a rectifier stage often processes high current. With reference to static losses, low conduction resistance (R_{ON}) devices reduce conduction losses in MOSFETs as shown by Equation (12). The gate drive losses involve the charge/discharge process of the gate capacitance and the power supply of the related drive circuitry. The electrolytic capacitor losses are less relevant; they are derived from the square of the RMS current flowing through the ESR of the capacitors (see Equation (16)). Although this is often considered a second-order effect, it influences the device's reliability and, consequently, that of the whole converter [56,57]. The inductive component losses are due to both the parasitic resistance of the inductor winding and magnetic losses; this necessitates an appropriate choice of components. Finally, auxiliary losses involve ancillary services such as fans and signal circuits.

3.2. Control Techniques and Topology Measures

A relevant performance improvement can be retrieved by suitable control techniques and topology measures. The current optimal partitioning consists of sharing the current among several paths; this allows lowering Joule losses because they are quadratic with respect to the current. This feature is exploited by interleaved circuits that also allow

a reduction in the ripple amplitude; using parallel conversion units allows the stand-by of some units when the power is much lower than the required one, achieving a flattened efficiency curve [53]. Appendix C provides an example of the analysis in a practical case.

The resonant mode consists of imposing the commutation of the power switches when voltage or current are null, realizing zero-voltage switching (ZVS) or zero current switching (ZCS), respectively. In this way, either the voltage or current are nullified in Equation (13). The resonant mode can be implemented by exploiting parasitic reactive components (such as leakage transformers, inductors, or MOSFET output capacitances) or by additional components.

The partial power conversion processes only a part of the total power; it highly increases efficiency, especially when the power to be converted is lower compared with the available power.

Finally, voltage range adaptation can be adopted when a wide input voltage range is required for the converter's operation. It consists of preconditioning the voltage by a supplementary pre-regulator stage.

The above considerations are the basis of the design of the circuits analyzed in the following sections, which are applied particularly to the supply of PEM electrolyzers.

4. Power Converters for Electrolyzers

The use of a power converter to supply the electrolyzer via a photovoltaic source allows the required voltage conversion and optimizes the operating point by tracking the maximum power during operation [65–67].

The power converter systems to interface a PV source with the electrolyzer can be divided into grid-connected systems and stand-alone DC/DC converters. The grid-connected systems are supplied by AC voltage requiring, in some cases, a line frequency transformer (LFT) (The line frequency transformer operates at a low frequency (corresponding to the grid frequency); although it guarantees the galvanic isolation, it is bulky compared to a high-frequency transformer). The stand-alone DC/DC converters can be divided into non-isolated and isolated converters. This section briefly describes the grid-connected systems; non-isolated and isolated converters are analyzed in Sections 5 and 6, respectively.

A representation of a grid-connected power conversion system is shown in Figure 7. The system is formed by a DC/AC converter supplied by the PV source, an AC/DC stage for the electrolyzer and, in some cases, a low-frequency transformer. This multiple conversion lowers the total efficiency and increases the cost compared to a direct DC/DC conversion. On the other hand, the grid can supply the electrolyzer despite the variations in the power produced by photovoltaic sources. To achieve green hydrogen at the rated power, the photovoltaic power must be higher than the one required by the electrolyzer; the remaining part can be used for other grid-connected services. The use of the grid, also supplied by a photovoltaic plant placed in a different point connection, guarantees the power to the electrolyzer that can be managed based on the hydrogen production requirements. At the moment, a significant part of commercial systems belongs to this category; however, hydrogen production by traditional methods is still relevant, in fact water electrolysis accounts for about 2% of the whole hydrogen supply [10].

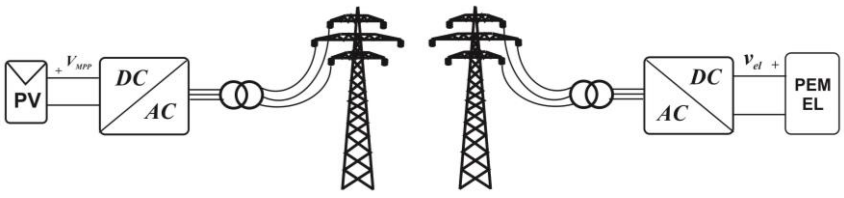

Figure 7. Structure of a grid-connected conversion system.

The high-power rectifiers connected to the grid play a crucial role; they transform medium voltage (MV) to a high DC current to supply electrolyzers. Commercial high-power rectifiers range up to 10 MW in power, supplying a current from 1.5 kA to 10 kA with a voltage of up to 1 kV. The main issues are related to their impact on the grid regarding power quality issues such as voltage imbalance, harmonic distortion, reactive power generation, and interference in the range of 2–9 kHz. Photovoltaic plants and wind turbines usually achieve the supply by RESs, interfaced to the grid by DC/AC inverters or AC/DC/AC converters, respectively. The grid behaves as a power transmission vector in which power can be integrated by auxiliary or traditional generation where necessary. The most used circuits are the 12-pulse thyristor rectifiers (12-THY) equipped with passive trap filters or with active shunt power filters to minimize distortion; the use of active front-end rectifiers provides a better power quality regulation capability. All these circuits adopt a line frequency transformer (LFT) in a configuration of wye-delta-wye to eliminate 5th and 7th-order harmonics, providing galvanic insolation. Another adopted rectifier is the 12-Pulse Diode Rectifier with a Multi-Phase Chopper (12-DRMC); it employs two uncontrolled rectifiers connected to a DC/DC converter equipped with IGBTs in an interleaved configuration. This converter requires notch filters at its input to suppress low-order harmonics. The twelve pulse thyristor rectifiers with active filter (12-THY-AF) are based on the 12-THY rectifier added with an active shunt filter at its input. Finally, the active front-end (AFE) rectifier is based on a three-phase IGBT bridge. A comparison of these four topologies is given in Table 1 concerning power quality, efficiency, control, reliability, and cost [39]. All these converters are implemented on a commercial scale and have been devised for alkaline electrolyzers; however, they could be employed for PEM electrolyzers. They are grid-connected circuits that can benefit from photovoltaic energy, as depicted in Figure 7.

Table 1. Comparison of the main features of high-power rectifiers employed in industry for hydrogen production.

Circuit	Power Quality	Efficiency	Control	Reliability	Cost
12-THY	poor	good	easy	very good	cheap
12-DRMC	neutral	neutral	neutral	good	cheap
12-THY-AF	good	neutral	difficult	neutral	neutral
AFE	very good	neutral	difficult	neutral	expensive

The comparison shows that each circuit has pros and cons; however, the AFE circuit can benefit from being updated with the emerging SiC MOSFETs instead of Silicon IGBTs [68].

Future developments are addressed with the suppression of the LFT by adopting a modular multicell rectifier in which the transformer operates at a high frequency in a DC/DC stage whose input is derived by an AC/DC converter. The whole structure is modular, and it is expected to be adopted for high-power rectification in the future [39]. Grid-supplied high-power rectifiers are also described in [38,39,44]. A comprehensive comparative analysis of the power converter topologies described above has been recently provided by [69]. The above-described circuits are grid-connected high-power rectifiers; hence, scaling to power around tens of kW to supply electrolyzers by photovoltaic plants is not feasible. For this reason, several topologies have been conceived, adopting MOSFETs or IGBTs as power switches instead of the controlled rectifiers and diodes. These converters, detailed in the following sections, can be supplied by the DC source encompassing suitable dynamic features to track the source variations.

5. Non-Isolated Power Converters

Non-isolated or transformerless circuits allow the use of smaller and cheaper converters with good efficiency. The most common topologies are step-down types, as the

electrolyzer requires low voltage, while the photovoltaic source is exercised with higher voltages to minimize the current delivered for the same power.

5.1. Basic Buck Converter

Introductory remark: This converter generates a square wave from a DC voltage by the commutation of a power switch. The square wave is then filtered, obtaining a lower DC voltage.

A classical buck converter is employed in [70,71]. The circuit is shown in Figure 8. The step-down ratio is equal to the duty cycle of the power switch D = ton/Ts (since *Ts* = *Ton* + *Toff*, the duty cycle is always between zero and one); hence, the output voltage is reduced and proportional to D as follows:

$$v_{el} = D\, v_{PV} \tag{23}$$

A suitable design of the LC filter minimizes the output ripple. The main drawback is the discontinuous input current, since the power switch is connected in series with the source; it would impose wide variations to the operating point of the PV generator (set on the maximum available power) that are limited by a parallel capacitance (drawn in gray in Figure 8). However, this capacitance modifies the converter's dynamic behavior [51]. The power switch is subjected to a current that is higher the more the duty cycle is reduced; this can be a problem if high input voltage reduction ratios are desired. Quadratic Buck converters assure a higher step-down ratio ($v_{el} = D^2\, v_{PV}$); in this case, with the same parameters, a reduced current ripple is obtained but with a higher voltage stress of the semiconductor [72]. In addition, the free-wheel diode supports the same current as the MOSFET, which is switched in the on–off transition of the MOSFET. Due to the parasitic inductance of the connections, overvoltages could be generated in the common inductor-diode-MOSFET node that can propagate to the load and source. The conduction losses of the power diode can be reduced by using a MOSFET instead of the diode. The obtained circuit is known as synchronous Buck. An example is proposed by [73]; the low conduction resistance of the MOSFETs allows for the reduction in the conduction losses, avoiding the drop voltage introduced by the free-wheel diode (Figure 9).

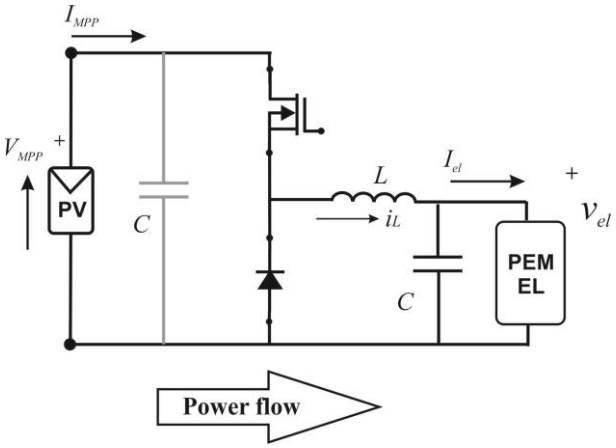

Figure 8. Traditional Buck converter.

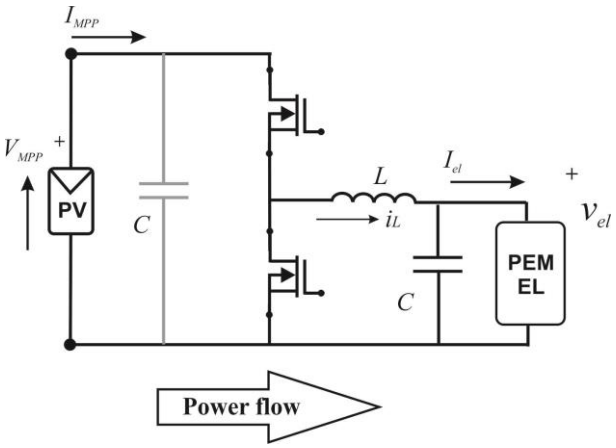

Figure 9. Synchronous Buck converter.

5.2. Interleaved Buck Converter

Introductory remark: This converter adopts parallel buck circuits to share the input current and reduce the conduction losses.

A solution to reduce the high input current flowing through the MOSFET and its ripple is given by the interleaved configuration in which many converters are parallel connected to share the current among legs, as shown in Figure 10. In this way, conduction losses through the power switches and inductors are lowered. In fact, considering that they are quadratic with respect to the current, the adoption of two legs halves these losses. The current sharing among legs is an effective way to reduce losses, especially when high currents have to be managed [74]. The number of parallel circuits can be further increased to make the efficiency curve flat as the power output varies, even for power much lower than the rated one, because of the distribution of losses; it may be more convenient to use only some branches [53]. An example is discussed in Appendix C. A suitable phase shifting of the carriers of the PWM modulator can minimize the output ripple. On the other hand, the circuit is more complicated, and current control is required to split the current among legs equally [74,75]. Finally, the presence of more legs is helpful in realizing fault-tolerant circuits since, in case of a fault of a power switch, the remaining legs can ensure the power supply to the electrolyzer.

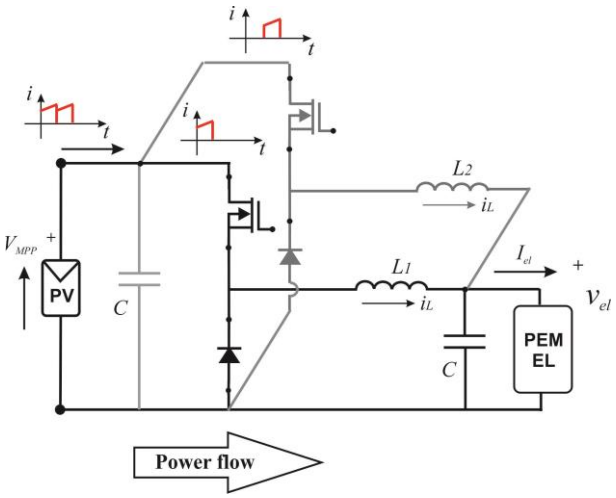

Figure 10. Interleaved Buck converter (red lines represent the current waveforms).

The above-mentioned advantages are summarized in surveys [42,43], where further topologies are addressed as follows: the interleaved buck can be improved by two coupled windings at the input stage enhancing the voltage ratio conversion [76], the

switching losses can be reduced by a Zero Current Transition of the power switches [77], and this approach corresponds to the nullification of the current I in Equation (13).

A practical application of interleaved topology is described in [78]; it proposes a three-leg interleaved buck converter supplied by the grid through a 12-pulse rectifier. The converter is conceived for a peak power of 400 kW. The same rated power is managed by a full-bridge step-down isolated DC-DC converter proposed by [79], in which the interleaved configuration is particularly convenient for an industrial water electrolyzer. A comparison of efficiency curves between a buck converter and an interleaved configuration is given in Appendix C.

5.3. Stacked Interleaved Buck Converter

Introductory remark: This converter is based on two buck circuits; only the former processes the power, and the latter is employed to minimize the voltage ripple.

The stacked interleaved proposed by [52] is a two-leg interleaved configuration in which a leg is devoted to the ripple compensation to preserve the electrolyzer [50]. The circuit is shown in Figure 11. The auxiliary capacitor C_{aux} stops the DC component of the current flowing through the inductor L_2; as a consequence, the leg connected to L_2 is exploited only for ripple compensation and can be designed for a lower power compared to the leg supplying L_1 that has to support the whole DC current required by the electrolyzer. Paper [52] also addresses the control issues of deriving the transfer function encompassing the dynamic model of the electrolyzer; this model plays a crucial role in the dynamic response of the converter.

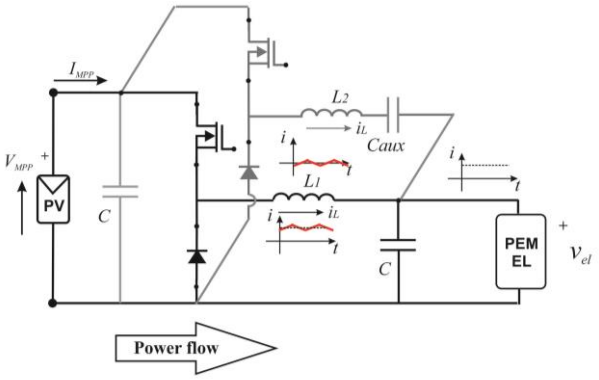

Figure 11. Stacked interleaved Buck converter (red lines represent the current waveforms)..

5.4. Three-Level Interleaved Buck Converter

Introductory remark: This converter operates like an interleaved buck. A capacitive divider partitions the input voltage, obtaining three voltage levels. The current is shared between two power switches to lower conduction losses (see Equation (12)) (Since the current flowing in a switch is halved, the losses in the same switch are reduced to a quarter).

The three-level interleaved buck converter proposed by [80] exploits the basic Buck topology in the double-phase interleaved version; the input voltage is halved by a capacitive divider and an analogous circuit is placed on the return path of the current. The circuit is shown in Figure 12. Each power switch with its free-wheel diode behaves like a traditional buck converter, each device is operated for half of the switching period by a phase displacement of the gate signals so that the thermal stress is reduced. Finally, the output current ripple is minimized, and fault accommodation can be provided as in an interleaved converter. Recently, a novel control algorithm for a TLIBC has been proposed to supply energy to a proton exchange membrane electrolyzer supplied by renewable sources. It is based on non-linear improved sliding model-based control, which improves dynamic response and robustness against parameter uncertainties [81].

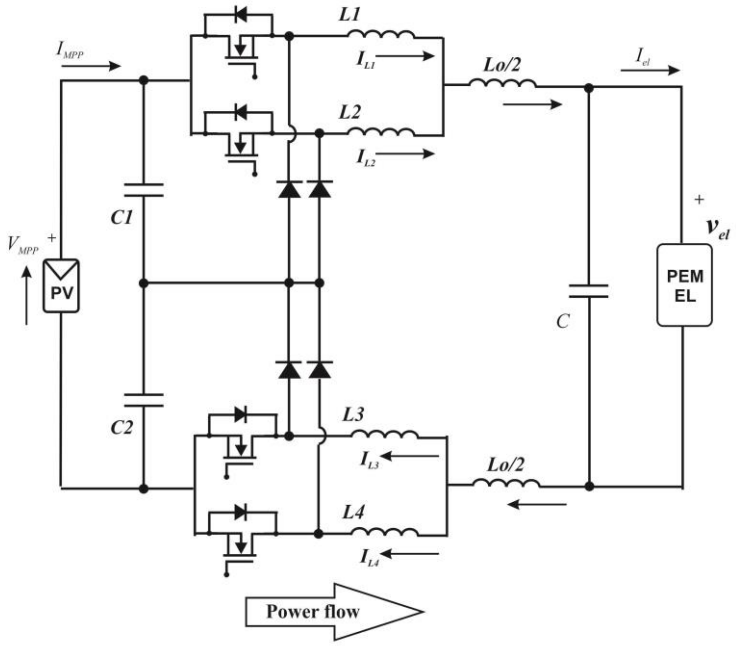

Figure 12. Three-level interleaved Buck converter.

5.5. Partial Power Conversion

Introductory remark: Unlike a traditional converter in which all power is processed, in partial power conversion (PPC), only a part of it flows through the converter.

A partial power conversion scheme is provided in Figure 13. With reference to a step-down conversion, based on the input voltage V_i and output V_o, an adjustable series voltage V_c is generated; this voltage is subtracted from V_i to retrieve V_o.

$$V_o = V_i - V_c \tag{24}$$

The converted power is limited to a lower level; this corresponds to the rated power of the converter stage which results in lower power compared to the whole power. In addition, in case $V_c \ll V_2$, a great part of the power does not need conversion to be delivered directly from the input.

$$\frac{P_c}{P_i} = \frac{V_c}{V_i} = \frac{\frac{V_c}{V_2}}{1 + \frac{V_c}{V_2}} \tag{25}$$

As a consequence, the total efficiency is increased as follows:

$$\eta = \frac{P_o}{P_i} = \frac{1 + \eta_c \frac{V_c}{V_2}}{1 + \frac{V_c}{V_2}} \tag{26}$$

where η_c is the efficiency of the converter stage; as an example, if the efficiency of the converter stage is $\eta_c = 0.85$ and $V_c/V_2 = 0.2$, a total efficiency of 0.975 is retrieved [53].

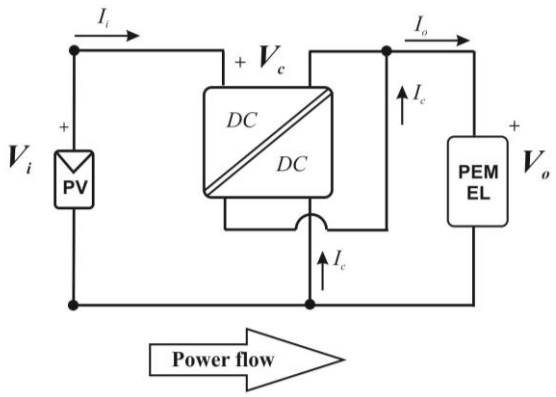

Figure 13. Partial power conversion scheme.

The advantages and some applications are summarized in [82], which proposes a PPC scheme to supply an alkaline electrolyzer. Although the rated power of the system is around 3.5 kW, the converter is designed to manage about 750 W. Similar results are obtained for supplying a solid-oxide electrolyzer/fuel cell converter where the rated power of the system is about 32.5 kW; in contrast, the converter is designed to manage about 3.6 kW. With reference to the limitations of PPC, it should be noted that the best efficiency results are obtained when the supply voltage is close to that of the load and that galvanic isolation between input and output cannot be achieved [82]. Although a transformer is required to implement PPC circuits, the converter connection does not provide galvanic isolation. Therefore, when safety requirements for both the source and the load, or also for any eventual human interaction with the devices, are mandatory, a different topology must be employed. Two examples of converters to be used in PPC are proposed by [83]; they are the Dual Active Bridge (DAB) and the Isolated Full Bridge (IFB), shown in Figures 14a and 14b, respectively. Both converters are analyzed since they show good efficiency with a limited component number. In the DAB, an inductor is employed to deliver the power to the output; it is charged and discharged based on the phase-shift angle of the half-bridge switching legs. The IFB converter exploits the duty cycle of the primary switches; the energy is transferred to the output port by an input inductor. The analysis proposed by [83] shows the best performance obtained by IFB in a wider operating region. More details on partial power conversion can be found in [84].

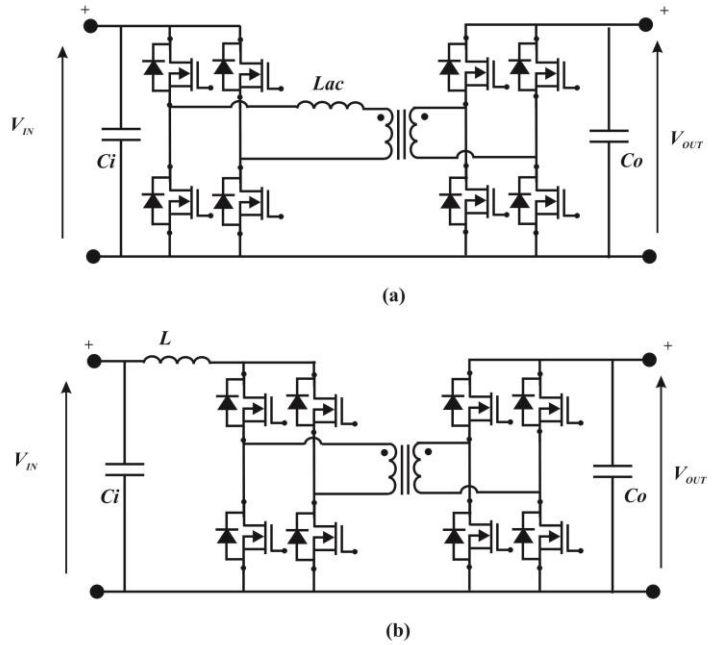

Figure 14. Converters employed in partial power conversion: (**a**) dual active bridge, (**b**) isolated full-bridge.

5.6. Direct Coupling

Introductory remark: The "direct coupling" between the source and the electrolyzer consists of a direct connection between the electrolyzer and the PV source without using a DC/DC converter as a power interface.

Within the last five years, the direct connection between a PV array and an electrolyzer has shown promise for low-power applications [85–87]; it is schematically shown in Figure 15. Most of the applications proposed in the literature concern small power plants [87–90]. The absence of the converter makes the system more economically viable [91] and provides an output voltage without any ripple [92]. On the other hand, it lacks the features allowed by the power interface such as maximum power point tracking, interfacing with existing plants, and partial shading management. In fact, since the source and the electrolyzer share the same voltage and current, the optimal matching can be retrieved at a single operating point. The literature proposes as a design criterion to obtain the optimal matching to set the maximum voltage of the PV source slightly above the rated voltage of the electrolyzer at the rated power [67]; however, throughout the year, the best operating points at maximum solar radiation represent a small percentage of the whole set. Conversion efficiency can be improved by a suitable reconfiguration of the photovoltaic source; some additional PV arrays are connected in parallel based on the solar radiation value. In this way, the number of operating points in which the optimal matching is reached is augmented, and an increased conversion efficiency is reached [93]. The reconfigurable PV source employed in direct coupling is drawn in Figure 16; the MOSFETs are operated as switches to connect in parallel auxiliary PV arrays. Further details on direct coupling can be found in [94].

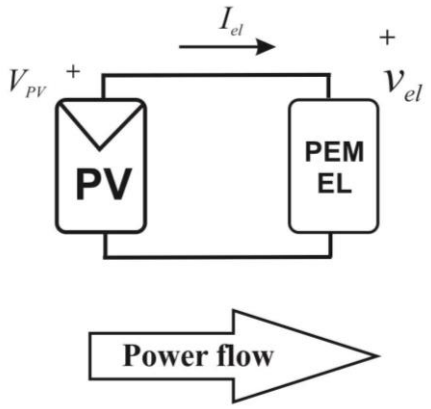

Figure 15. Direct coupled connection.

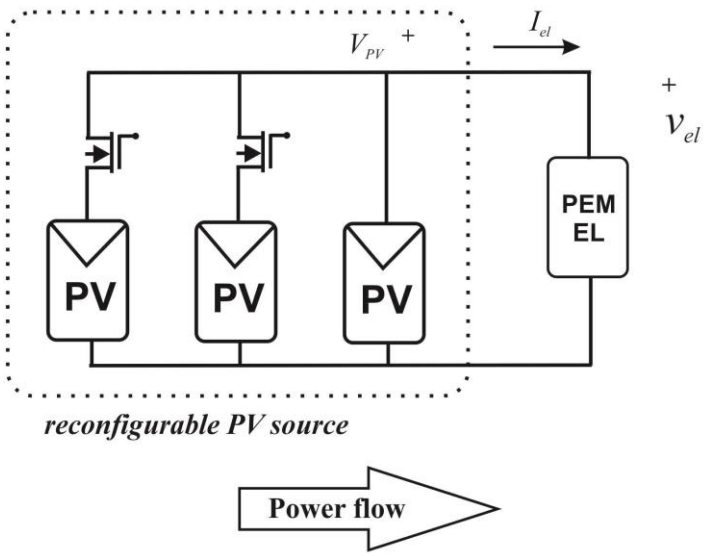

Figure 16. Direct coupled connection with reconfigurable PV source.

5.7. Feature Comparison of Transformerless Converters

The main features of transformerless converters are summarized in Table 2. The basic buck is the simplest but shows poor performance; the stacked buck is similar. However, it allows for reducing output ripple. The interleaved buck adopts a high number of devices; on the other hand, efficiency increases as well as the minimization of the output voltage ripple; it is a fault-tolerant converter since, in case of a power switch failure, the remaining legs can continue to operate. The three-level interleaved buck is also fault-tolerant, improving the step-down ratio. Finally, partial power conversion requires a more complicated circuit, including a transformer; however, a significant part of the input power does not need conversion to be delivered directly from the input, and it achieves high efficiency.

Table 2. Comparison of the main features of transformerless converters.

Converter	Figure	Ref.	Number of Devices	Efficiency	Step-Down Ratio	Current Ripple	Power Density
Basic Buck	7	[54]	low	low	low	high	high
Interleaved Buck	9	[72,73]	high	high	low	low	fair
Stacked Interleaved Buck	10	[55]	low	low	low	low	fair

Three Level Interleaved Buck	11	[78]	high	good	good	low	fair
PPC	12	[80,81]	high	very good	good	low	high

6. Isolated Power Converters

Introductory remark: These converters generate a square wave voltage by exploiting different inverter input stages. This voltage is applied to a transformer; then, it is rectified and filtered to extract the mean value. The obtained DC voltage supplies the electrolyzer according to the block diagram shown in Figure 17.

The isolated topologies allow for a high step-down ratio by a high-frequency voltage matching transformer; additionally, they provide a galvanic isolation of the primary and secondary side. The magnetic coupling given by the transformer allows multi-ports circuits to interface with other sources, such as fuel cells, or auxiliary storage systems [7]. Due to the inherent nature of the transformer, which needs to be supplied by an AC voltage, the general structure of these converters to retrieve a DC/DC conversion consists of (a) an inverter stage, (b) the insolation transformer, (c) a rectifier, (d) an output filter. The DC supply is converted into an AC waveform by the inverter stage. The DC to AC conversion is performed at a high frequency, allowing a reduced transformer size; the secondary voltage is converted into a DC voltage by the rectifier stage, and the output filter provides a suitable reduced ripple level [95].

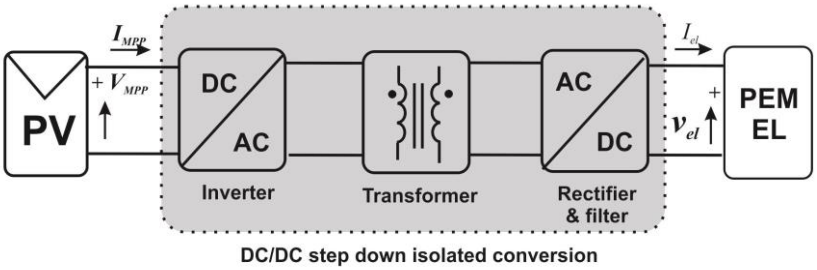

Figure 17. Block diagram of a DC/DC conversion obtained through insolated converter.

The inverter stages can be classified into push-pull (PP), half-bridge (HB), and full-bridge (FB) topologies. The related circuits are drawn in Figure 18.

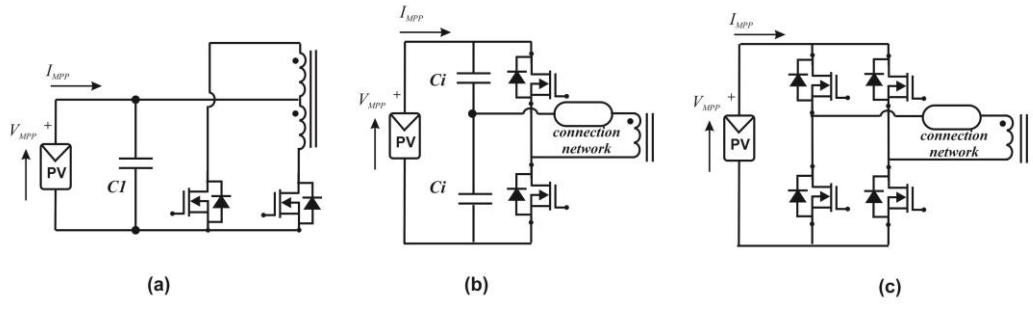

Figure 18. Inverter circuits employed in insolated converters: (**a**) push-pull, (**b**) half-bridge, (**c**) full-bridge.

The PP topology needs only two low-side power switches (the low-side switches are connected to the ground reference potential); as a consequence, the driver circuit does not need a high-side floating supply. On the other hand, two primary windings are required and a good matching of the switches is necessary to prevent different conduction times, since it results in the saturation of the transformer core. The HB converter uses a capacitive divider as the second leg. It reduces the number of required switches compared to FB

and, consequently, the related losses and the drive circuitry. The voltage applied to the transformer is halved, and a lower isolation of the transformer's primary voltage is required. This topology assumes that the voltage at the middle point of the capacitive divider is constant; a suitable sizing of the capacitors it required to obtain it. Since this voltage depends on the current supplied by the capacitive divider during the commutations of the active leg, this topology is commonly used for a power range of around 1 kW. The FB circuit adopts four complementary switches, which allow for higher power compared to HB and a higher voltage to be applied to the transformer. A suitable circuit can connect the inverter stage and the transformer. An inductance is adopted to achieve a phase-shifted zero-voltage-switching (ZVS) PWM inverter; otherwise, a series of an inductor and a capacitance gives (exploiting the magnetizing inductance of the primary also) an LCL series resonant inverter. A comparison among soft-switching solutions is given in [96]. In general, soft-switching performance depends on input voltage; it must be taken into account when managing PV sources where the voltage is tied to solar irradiance [97]. An LCL resonant converter, employing as a connection network a "T" resonator made of two inductors and a capacitor, is presented in [98].

The three-phase configurations can be used to improve the losses distribution in the converter increasing the power converter ratings; however, these topologies excessively augment the number of components [95].

The output rectifier provides the DC voltage output. The output filter has to minimize the residual ripple. The rectification can be realized by single-phase FB four-diodes configuration or by a center tap output transformer with two diodes as the current doubler. The efficiency conversion of the rectifier stage is crucial since it is interested in high currents and the drop voltage across diodes increases losses. In addition, the reverse recovery losses in the rectifier diodes need suitable design for their minimization. Some practical realizations are analyzed in the following sub-sections.

6.1. Push-Pull Inverter

A push-pull DC/DC converter for electrolyzers supplied from photovoltaic sources is proposed by [99]; the circuit is drawn in Figure 19. The converter is designed for 5 kW of the rated power, and design guidelines are given. The circuit shows the typical advantages of the push-pull, such as using two low-side connected power switches, the absence of voltage equalizing input capacitors, and simple hard-switching driving with PWM control, air-forced heatsinks to perform cooling. On the other hand, the transformer needs a center tap both at the input and output; the hard switching reduces efficiency, and primary devices have to support twice the input voltage in the blocking state.

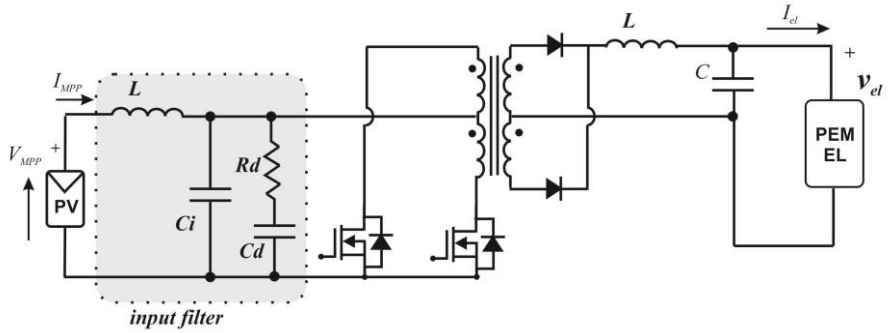

Figure 19. DC/DC isolated step-down converter using push-pull inverter.

Some additional issues concern the specific application with a PV source as supply and the electrolyzer as load. The PV source and the load are non-linear devices. The PV source voltage versus current characteristic depends on solar irradiance and temperature. To avoid the operating point of the PV source being influenced by the input current rip-

ple imposed by the converter, an input filter is required. In fact, the pulsated current creates wide input voltage variations, moving the PV operating point from zero (open circuit condition with both switches off) to the point imposed by the maximum current. The input filter can minimize these variations; however, its impedance must be compatible with the input impedance of the converter to guarantee stability [100]. As a design criterion, the input filter impedance is set 10 dB lower than the converter's minimum input impedance. This input filter exploits a series inductance and a parallel of damped and undamped capacitances. As power devices, the converter employs IGBTs switched at 50 kHz, resulting in an output ripple frequency of 100 kHz. Finally, the efficiency, measured at a maximum output power of 2.5 kW, is around 90%. Paper [101] deals with the same circuit addressing the converter control in detail. The control system aims to perform the maximum photovoltaic power tracking and electrolyzer current control; in this way, the converter behaves as a current source proportional to the hydrogen production. In addition, the two cases corresponding to a PV power that does not meet the electrolyzer power needs and a PV power exceeding the requirements of the electrolyzer are taken into account. Both [99,101] provide experimental verification of the theoretical model and the results obtained by the simulation.

6.2. Half-Bridge Inverter

A DC/DC converter based on a half-bridge circuit is proposed by [102]. As a rectifier, a full-bridge active rectifier is adopted. The circuit is shown in Figure 20. A Zero Voltage Switching (ZVS) operation is achieved by the phase shifting operation of the active rectifier; it allows using non-dissipative capacitive snubbers connected to the two inverter switches that are operated at a constant frequency. The typical disadvantage of these circuits consists of a time interval in which a quantity of energy goes back to the power supply. It could be minimized by increasing the capacitance values; however, it implies an increase in weight and cost. Instead, the paper [103] proposes two additional switching states of the rectifier switches to reduce the energy return interval, maintaining the main feature of regulating the output voltage in a wide range by the phase-shift of the rectifier switches. The proposed prototype adopts MOSFETs and series diodes for the rectifier; however, as claimed by the authors, higher efficiency can be retrieved by reverse-blocking IGBTs or fast thyristors. A 1 kW converter has an experimentally verified performance; the efficiency curve is not given.

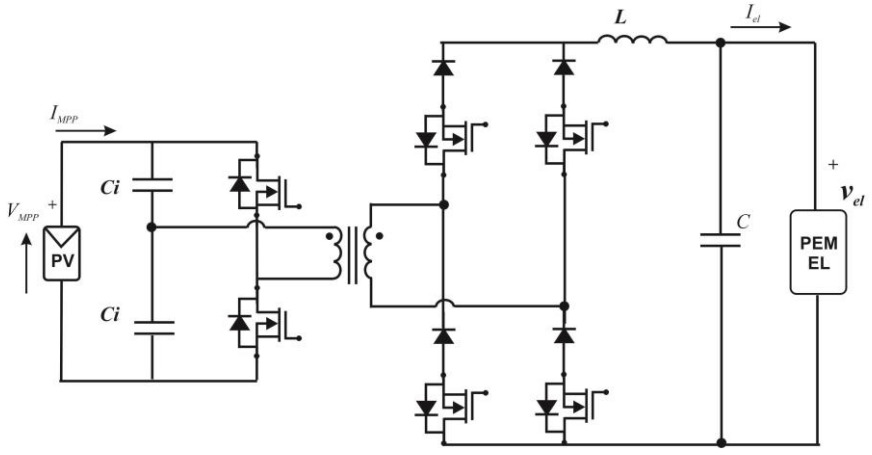

Figure 20. DC/DC isolated step-down converter using a half-bridge inverter.

A DC/DC isolated converter employing a three-level neutral point clamped (3L_NPC) inverter and a current double rectifier is proposed by [104]. The circuit is provided in Figure 21. The output stage employs a current doubler rectifier (CDR). The

three-level topology allows switches blocking voltage twice reduced compared to the two-level inverter. The ZVS of the inverter is achieved by the parasitic elements of the components (mainly free-wheeling diodes capacitance and leakage inductance of the transformer) and the PWM control algorithm. Only two independent PWM channels are required since the dead time generator and a common signal blocking system are implemented by discrete logic circuits. The ZVS condition requires a relatively large leakage inductance and a constraint on the dead time that must be lower than the time necessary to exploit the leakage energy. The CDR circuit exploits a single secondary transformer winding and two mutually coupled inductors. Compared to the traditional full-bridge rectifier, losses in diodes are halved; compared with the full wave rectifier with two diodes and a center tap transformer, the CDR exploits a simpler transformer. This feature allows the ripple current reduction toward the electrolyzer [103]. A further optimization could be the design of a fully integrated magnetic structure encompassing the insolation transformer and the two coupled inductors as described by [105]. The proposed circuit shows an efficiency that is approximately 95% experimentally verified.

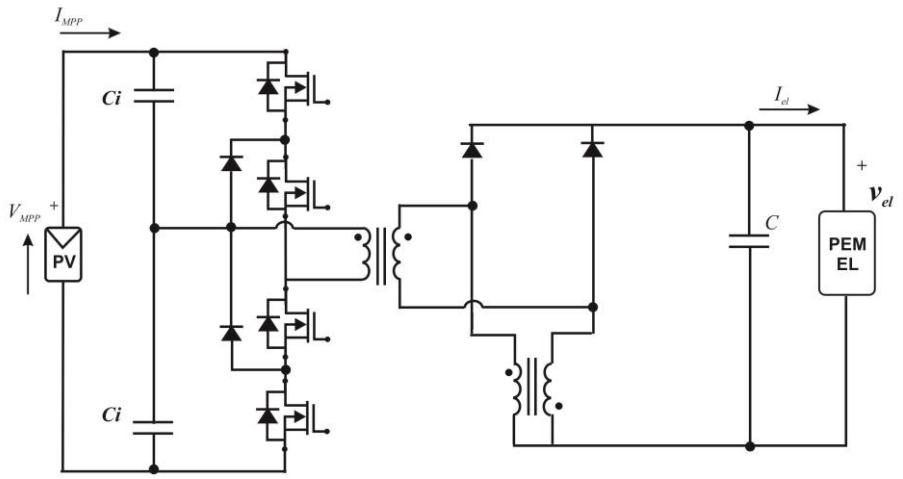

Figure 21. DC/DC isolated step-down converter using a three-level half-bridge inverter.

6.3. Full-Bridge Inverter

The full-bridge inverter is the most commonly used inverter when higher power is required. Paper [45] proposes a Multi-Resonant Converter (MRC) with a center-tapped rectifier. The circuit is exploited as a constant current source. The characteristics parameters are the output admittance and the relative switching frequency variation over the frequency operating range. The output admittance G is defined as the output current variation I_{el} over the DC conversion ratio M: $G = \Delta I_{el}/\Delta M$. This value is expected to be as low as possible, meaning that a low variation in the output current for constant switching frequency occurs. Four different solutions are compared, MRC, LLC, LCC, and LLC-T. The MRC in the middle of the operating range has the lowest admittance, whereas the switching frequency variation in the MRC is higher than the LCC and LCC-T converters and lower than LLC. The proposed circuit is shown in Figure 22. It exploits, as a resonant network, the MOSFET output capacitances *Co*, an inductor *Lr*, and externally added capacitors *Cdr* across the rectifier diodes. When a diode is reverse-biased, its capacitor is reflected by the transformer to the primary side. The resonant network exploits the major parasitic parameters such as the transformer leakage inductance and the rectifier capacitance. Four operating modes are recognized depending on the resonance on a specific part of the resonant network, A suitable choice of the capacitance *Co* allows a resonant voltage transition on the bridge; otherwise, switching losses are increased. A detailed analysis of all modes of operation can be found in [106]. Experimental results on a 1,2 kW

prototype showed a minimal frequency variation (210–219 kHz), assuring a constant current of 36 A, varying the output voltage from 34.42 V to 18.78 V with a DC link voltage of 310 V. Finally, the efficiency curve shows an increasing trend, with the output power reaching 94%. It demonstrates that such circuits can retrieve a flat efficiency curve.

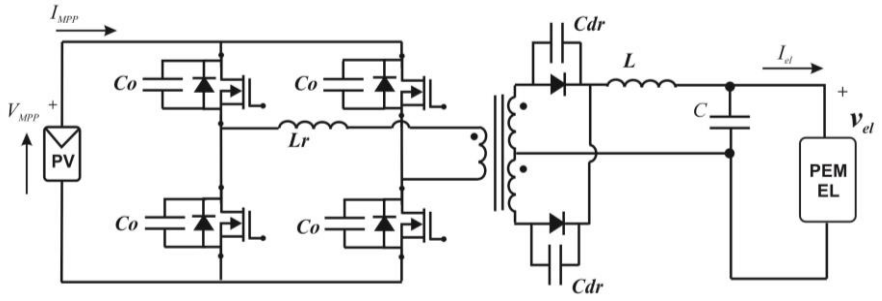

Figure 22. DC/DC isolated step-down converter using a multi-resonant converter with a full-bridge inverter and center tapped rectifier.

A Full-bridge inverter with a current doubler rectifier has also been proposed in [107]. The circuit is shown in Figure 23. A zero-voltage switching is implemented in the full bridge by introducing a time delay between the commutation of upper switches; low R_{ON} MOSFETs are used. As a resonant network, an inductor with the leakage transformer inductance is exploited, whereas the capacitive part is given by the output capacitance of the MOSFETs and an additional capacitance. The current doubler rectifier is equipped with fast recovery diodes requiring a single-winding secondary transformer. The efficiency, experimentally measured on a 1 kW prototype, shows a maximum value of about 96% around 800 W and a slight decrease of up to 94% in the rated power.

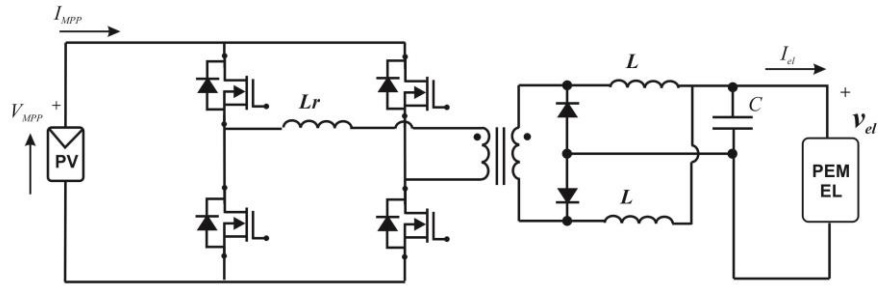

Figure 23. Full-bridge inverter with a current doubler rectifier.

6.4. Full-Bridge Converters with Pre-Regulator Stage

A comparison among full-bridge soft-switched FB DC/DC converters is provided by [108]. Three topologies are considered: (a) fixed-frequency LCL series resonant converter with capacitive output filter, (b) fixed-frequency LCL series resonant converter with inductor output filter, (c) fixed-frequency phase-shift controlled zero-voltage-switching full-bridge PWM converter. The three circuits are designed for a rated power of 2.4 kW to be used in interleaved connection (meaning three identical circuits supplied by the same DC source). Each circuit is phase-shifted by 120°, to manage a total power of 7.2 kW, reducing the input current ripple. The switching frequency is set to 100 kHz. The converters are designed to work with an input and output voltage ranging from 40 V to 60 V and a maximum delivered current of 40 A. Concerning Figure 18c, the LCL SRC with capacitive output filter employs as a resonant network a series of capacitor-inductor and an auxiliary inductor *Lr* parallel connected to the secondary side of the transformer; only an

output capacitor is exploited as a filter. The LCL SRC series resonant converter with an inductor output filter uses the same resonant network and a LC filter at the output of the rectifier. The phase-shift controlled ZVS adopts an inductor as a resonant network, together with the leakage inductance of the transformer and an LC filter at the output of the rectifier. All circuits use capacitors across the terminals of the FB devices. The first two circuits ensure ZVS for all the switches of the FB inverter; the peak current through the switches diminishes with load current. The third circuit realizes the ZVS for the switches and achieves a reduced peak current stress compared to the resonant converters; however, snubber circuits are required across the output rectifier since the diode junction capacitance with the leakage inductance of the transformer resonates generating voltage ringing. As a result, the LCL SRC series resonant converter with an inductor output filter is preferred to the other two converters because it also offers the highest efficiency, no duty cycle loss (meaning no contemporary conduction of all the output rectifier), and no ringing issues on the rectifier. In addition, this circuit requires a higher value of the resonant inductor, making its realization easier since it includes the leakage inductance of the transformer. A pre-regulator stage is added to overcome the drawback of this circuit, which is the lack of the ZVS for maximum input voltage. In general, this additional circuit helps assure the ZVS for input voltage variations, and, in particular,, it avoids the use of a small value for *Lr*, which is difficult to obtain in practice. The adopted circuit is a zero-voltage transition (ZVT) boost converter with a snubber cell consisting of an inductor, a capacitor, an auxiliary switch and two auxiliary diodes; since all the switches are turned on and off under exact or near ZVS and/or ZCS, there is no additional voltage and current stresses on the main devices, resulting in a very high efficiency [109,110]. The circuit is drawn in Figure 24.

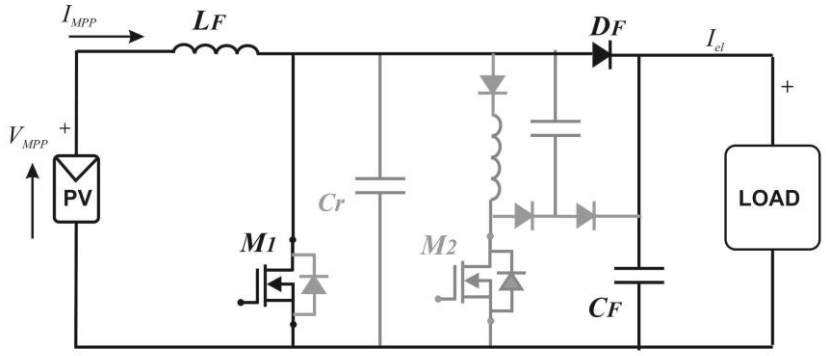

Figure 24. Pre-regulation boost converter stage with an additional network to achieve ZVS and/or ZCS, (in gray lines).

6.5. DCX Converters

The pre-regulated stage is also proposed by [111] with DCX converters. The DCX converter is an isolated resonant converter operated in an open-loop with soft-switching at a resonant frequency; it is considered a DC/DC transformer [112,113]. The structure is analogous to that shown in Figure 17. Paper [111] provides a detailed comparison of DCX topologies expressly conceived for PV to electrolyzer applications, showing that DCX converters promise to be a very efficient solution in performing larger voltage conversion ratio requirements with DC voltage matching, high efficiency, and high-power density. Four basic converters are analyzed; they adopt as inverter stage the half-bridge and the full-bridge diodes, whereas, as a rectifier, a full-bridge diode and a center-tapped circuit are chosen. The soft switching is realized by a resonant network formed by a series connection of inductor and capacitor, together with the leakage inductance of the transformer, obtaining an LLC resonant converter. The DCX converter can also be exploited by

a modular structure in an input-series output-parallel (ISOP) connection. The converter is always operated at a fixed frequency corresponding to the resonant frequency. In this operating point, the gain is independent of the load. A loss analysis shows that the best efficiency is achieved by the half-bridge center-tapper (HB-CT) configuration; it exhibits a low slope gain curve. The experimental realization is designed for 5 kW rated power, an input voltage of 600 V, and an output of 200 V operated at 200 kHz switching frequency. Since the DCX converter operates in an open loop, an interleaved buck converter is provided as a pre-regulation stage. The control scheme contains an inner control loop to control the current injected into the electrolyzer. Concerning efficiency, the HB-CT converter lies between 98.6% and 98.5% with a maximum of 99.2%, whereas the interleaved buck converter presents a maximum of 99.2% at 4.5 kW; as a consequence, the global system has an efficiency higher than 96% over the whole power range, with a maximum of 98.2% at 4.5 kW.

6.6. Full-Bridge Converters with Multi-Port

The multiport converter allows for reducing the number of energy conversion stages when an auxiliary energy storage/generation system has to be added; the ports are magnetically coupled by the transformer. These features are of interest for improving the overall efficiency, cost, and flexibility of the hydrogen buffers-based systems. Paper [114] proposes a multiport DC/DC converter for hydrogen-based energy storages with three ports, a bidirectional VSI port, a unidirectional VSI port, and a unidirectional quasi zeta source inverter (qZSI) port.

By adding a fuel cell (FC) as a generator, two distinct operation modes are recognizable, hydrogen generation (EL operation mode) and generation by a fuel cell (i.e., FC operation mode). In the EL operation mode, the converter behaves as a step-down DC/DC converter with a half-bridge inverter and current-doubler rectifier (Figure 25). In the FC operation mode, the converter works as a boost DC/DC converter and the power flows from the FC to the high-voltage DC bus exploiting the HB free-wheel diodes. The simultaneous conduction of both switches of the same phase leg of the qZSI is exploited (shoot-through switching) to store the magnetic energy in the side inductors L1 and L2 without short-circuiting the DC capacitors. This switching state is not allowed for the traditional voltage source converters because it damages the inverter [115]. A similar circuit that integrates a battery to improve the response time of the FC is proposed by [116]. The battery is parallel connected to the transversal capacitance *Ct*. Compared to the previous realization, additional operating modes of the FC mode consist of the power delivered both by FC and battery, or only by FC or only by the battery. In addition, in [116], a HB three-level inverter is adopted; it allows loss reduction of about 25% in the switches.

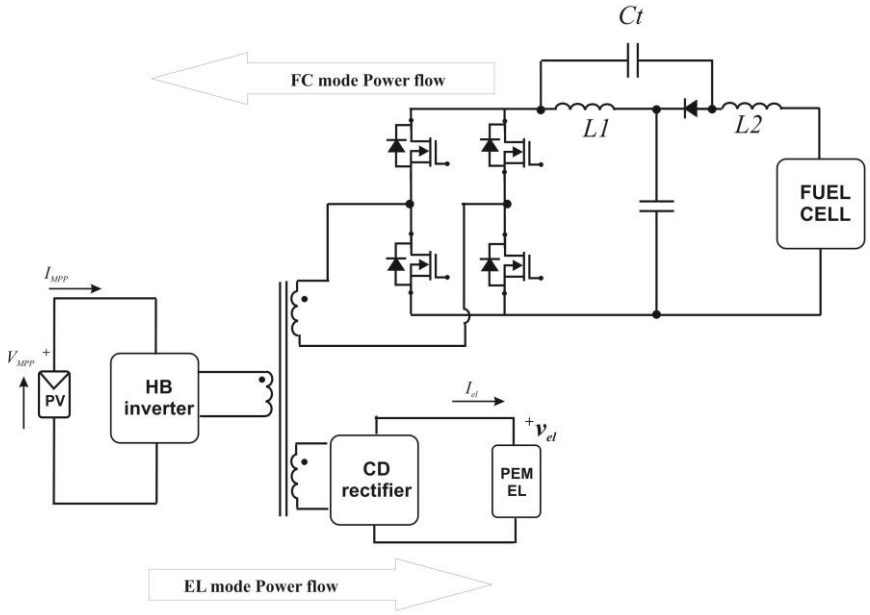

Figure 25. Multiport converter.

6.7. Feature Comparison of Isolated Converters

The main features of isolated converters are summarized in Table 3. All these circuits exhibit a good step-down ratio thanks to the transformer that worsens the power density. On the other hand, its cost and weight can be reduced by raising the switching frequency as expected in the future. The transformer allows multi-port configuration to exchange energy with storage systems.

Table 3. Comparison of the main features of isolated converters.

Topology	Figure	Ref.	Number of Devices	Efficiency	Current Ripple
Push-pull	18	[99–101]	low	low	fair
Half-bridge with full-bridge rectifier	19	[102]	fair	fair	fair
Full-bridge inverter with current doubler rectifier	22	[107]	high	good	fair
Full-bridge converters with pre-regulator stage	22,23	[108]	high	very good	fair
Two-stage with DCX	16	[111]	high	very good	fair

Table 4 provides a quantitative comparison of the most promising converters. It contains conversion systems conceived for PEM electrolyzers or which can be used for such systems. The following parameters are specified: circuit topology, number of devices, rated power, efficiency, and type of control. The cost, on the other hand, is not shown in the cited papers; however, it depends on the number of devices and the transformer, if used. All converters are prototypes or concepts. In general, ZVS allows higher efficiency and the adoption of a pre-regulator stage.

Table 4. Comparison of power supply converters for PEM electrolyzers.

Topology	Reference	Number of Devices	Rated Power	Efficiency	Control
Single-stage	[73]	2 MOSFETs	50 W	≈95%	PWM/ZVS
Isolated	[99]	2 MOSFETs 2 diodes	5 kW	≈90%	ZVS
Isolated (LCL-SRC with capacitive output filter)	[96]	4 MOSFETs 4 diodes	7.2 kW	≈90.8%	ZVS
Isolated (LCL-SRC with inductive output	[96]	4 MOSFETs	7.2 kW	≈90%	ZVS

filter)		4 diodes			
Isolated (full-bridge with inductive output filter)	[96]	4 MOSFETs 4 diodes	7.2 kW	≈89.8%	PWM/ZVS
Multi-phase Interleaved	[117]	2 MOSFETs 2 diodes	2.5 kW	≈96%	PWM/ZVS
Three-phase interleaved parallel LLC	[118]	6 MOSFETs 12 diodes	6 kW	≈93.1%	ZVS
Two-stage with LLC-DCX	[111]	2 MOSFETs 2 diodes +(2 MOSFETs 2 diodes) [1]	5 kW	>98%	Variable frequency/PWM [1]

[1] pre-regulator stage.

7. Perspectives

From a power electronics perspective, the future prospects of green hydrogen produced by photovoltaic sources mainly concern three areas, converter circuits, electronic components, and system issues.

7.1. Converter Circuits

From the analysis provided in this paper, it can be recognized that the literature shows many recent contributions to power converters devised for PEM electrolyzers' supplied by photovoltaic plants. Results are encouraging, especially for low-medium power conversion circuits where some converters, such as the LCL SRC series resonant or the HB-CT, exhibit high performance and relevant efficiency; however, the proposed circuits are prototypes or concepts. These converters permit high switching frequencies, minimizing the size and cost of reactive components. The modularity of these circuits allows parallel interleaved connections, increasing the managed power and ripple cancelation. These features represent an excellent standpoint for a short-term solution implementing green hydrogen production as a decentralized generation, locating the electrolyzers supplied by renewable energy in proximity to end-user consumption points, as energy storage for fuel cells connected to the local electrical grid, or for power-to-gas use.

7.2. New Power Devices

Power converters can benefit from further performance enhancement due to power static switches based on wide-bandgap (WBG) semiconductors. Four main categories are recognizable, GaN, SiC, diamond, and β-Ga_2O_3. Their performance, compared to silicon, is shown in Figure 26. In general, these materials are promising for better performance by power switches; in fact, they exhibit a higher breakdown electric field (allowing higher voltage for a device in off state), higher mobility (lowering switching losses due to the reduced turn-on and turn-off time) and, in some cases, better figure of merit BFOM and JFOM. The figure of merit represents a metric for evaluating efficiency considering both conduction and switching losses.

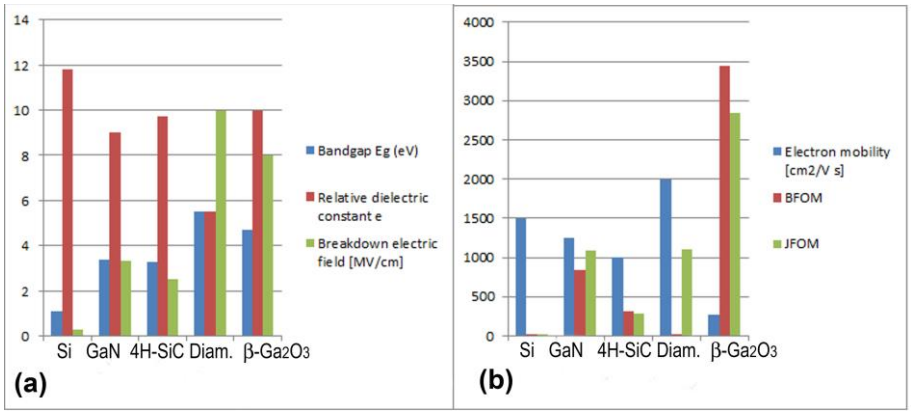

Figure 26. Performance comparison of wide-bandgap (WBG) semiconductors: diagram (a) contains the value of the bandgap, the relative dielectric constant and the breakdown electric field, (b) contains the electron mobility, the B and J figure of merits.

Diamond and β-Ga_2O_3 show features that outperform other devices; however, at the moment, no relevant availability on the market is noted. A study focused on high-voltage and medium-voltage converters showed that β-Ga_2O_3-based devices on diamond substrates can reduce converter losses [119].

Silicon carbide (SiC) and gallium nitride (GaN) exhibit sufficient performance for the realization of high-voltage switches for power converters and exhibit a high level of maturity and industrialization. At present, SiC exploits high-voltage-oriented power devices, covering voltage classes from 650 to 1700 V, having the availability of power modules with integrated gate drivers and temperature sensing. Conversely, GaN can cover a voltage range from 15 V to 1200 V, even if the diffusion of such devices is almost entirely limited to the 650 V range. Considering the 650 V range, i.e., the most suitable for the converter analyzed in this paper, a comparison based on the figure of merit (FOM), defined by the multiplication between the conduction resistance R_{ON} and the total gate charge Q_G, shows the best performance of GaN-based devices. The FOM accounts for both conduction and switching losses. In addition, the dynamic performance of GaN-based devices is better, obtaining lower turn-on delay time ($t_{d\text{-}on}$), turn-off delay time ($t_{d\text{-}off}$), rise time (tr), and fall time (tf). From a cost standpoint, the traditional Silicon devices are still the cheapest, with an increase of 30% for GaN and 50% for SiC discrete devices, however, the possibility to work at higher switching frequencies would allow for less bulky and cheaper passive components [120].

Concerning future perspectives, MOSFET and IGBT devices show peculiar characteristics such as the higher commutation speed of MOSFETs (since the conduction is based on unipolar charges) and the improved robustness of IGBTs (whose operation exploits bipolar junctions). In general, there are many expected advantages given by wide-bandgap semiconductors. Compared to silicon devices, SiC and GaN power transistors are smaller because of the reduced die area; it allows a higher breakdown field (>3 mV/cm), and higher temperatures can be sustained due to the wider energy bandgap. In addition, conduction losses are lessened due to the lower conduction resistance; as a consequence, the overall efficiency achievable by the power converter is improved with the further advantage of requiring cheaper heatsinks and cooling systems. From a dynamic point of view, the reduced input capacitance and gate charge improve dynamic performance, allowing a higher frequency of operation and, consequently, reducing reactive components (inductors and capacitors sizes). At the moment, Si-IGBT devices are employed for higher power; however, in the future, both MOSFETs and IGBTs can be updated with new materials, maintaining their inherent features. SiC domain ranges for blocking voltages higher than 1200 V, in the range from 400 V to 1200 V, exist for both GaN and SiC, whereas, for voltages lower than 400 V, GaN devices are dominant. Future applications of IGBTs will always involve high powers with relatively low frequencies,

but they will be enhanced by new semiconductors; the same is the case for gate turn-offs (GTOs) and silicon-controlled rectifiers [120]. On this basis, GaN devices are expected to find applications in all converters described above, such as resonant LLC and soft-switching or zero-voltage-switching (ZVS) topologies, and particularly, in a half-bridge configuration, where the retrofit with GaN devices allows for higher frequencies and efficiencies.

The current challenges regarding the converters' retrofits regard the increased role of parasitics requiring the suitable layout of the circuit and power modules with integrated drivers, an increase in frequency-dependent magnetic losses with a need for suitable core materials, and new EMI filters. Finally, GaN device parasitics such as threshold voltage, conduction resistance, and input capacitance vary with the frequency [121] and address the suitable measurement systems for characterization [122–124]; this aspect is essential to the design of resonant converters exploiting parasitics. These issues can be faced during the design stage and do not significantly influence the benefits brought about by the new devices. Upgrading existing topologies with newly available devices can be implemented as early as in the next few years, so it is expected that commercial-scale deployment will occur using the new devices.

At the moment, two GaN-based converters have already been proposed in the literature; a stacked interleaved buck converter [125] and different solutions for a DC-DC converter for a 10 kW PEM electrolyzer show an efficiency of around 98% at the rated power [126].

7.3. Hard-to-Abate Sectors

The considerations described so far show excellent technological maturity for power converters that can be used to produce green hydrogen from photovoltaics. However, as Figure 4 shows, the converter is only one element in the conversion chain that begins with the photovoltaic source and ends with the electrolyzer. Some issues concerning hard-to-abate sectors are technical-economics, other concern policy.

The cost of the photovoltaic cells has been strongly reduced; in 1975, it was about 100 $/kW, reduced to about 10 $/kW in 1990, it reached 1 $/kW in 2014, showing a further decreasing trend. Conversely, the modules conversion efficiency is increased, rising from 8% in 1980 to 15.2% in 2012 [127].

For electrolyzers, however, there are many factors to consider requiring cost-effective solutions. At the moment, PEM electrolyzers are more expensive, showing a cost of 1300–1500 $ per KW [128]; the optimization of cell operation conditions, such as higher pressures and temperatures, can augment the efficiency of electrolyzers without degrading membrane performance and durability-lowering costs [129]. The stack performance can be improved by redesigning stacks for a higher current density and reducing the reliance on precious materials. Other issues concern the balance of the plant, which encompasses the reduction of hydrogen compression energy, the optimization of storage, and the renewable energy integration [128].

In the future, the cost reduction in electrolyzers will play a crucial role. Cost-effective and efficient green hydrogen production through electrolysis must consider capital expenditure (CAPEX) and operational expenditure (OPEX). The former depends on materials such as thinner membranes, active catalysts, and reduced raw material; the latter depends on water quality, high-pressure operation, and maintenance. Other issues involve storage, transportation, and distribution [128]. Finally, a further challenge for green hydrogen production concerns the trade-off between augmenting the efficiency of the whole conversion chain and minimizing costs [130].

Beyond technical and economic considerations, there are policy aspects to be considered; they also involve the need for standards [131] and social aspects related to safety (risks that can arise from its high-flammability range, potentially leading to explosions) [132]. Another issue is the low number of recent strategic research assessments concern-

ing the commercialization of green hydrogen in the literature compared to the remarkable increase in the number of publications dealing with PEM technology [128].

8. Conclusions

The power converters conceived for supplying polymer electrolyte membrane (PEM) electrolyzers from photovoltaic sources proposed in the recent literature have reached a remarkable efficiency and overall performance. They are expected to be further updated and improved by the availability of GaN and SiC devices, which will provide higher efficiency, robustness, and power density relative to their silicon counterparts. Most solutions are ready-to-market; however, they are still not counterbalanced by the equipment available on the market. On the other hand, considering the entire production chain, photovoltaic sources have seen a sharp reduction in cost and an increase in conversion efficiency while electrolyzers still need research and investments to be competitive.

To incentivize the deployment of green hydrogen production facilities, cost reduction is key; it particularly concerns the electrolyzers. An appropriate policy of economic incentives can help address the initial cost of the plant, especially for distributed generation.

There are also hard-to-abate sectors, including standards and social aspects related to safety.

This scenario appears favorable to the spread of short-term solutions, including green hydrogen produced by electrolyzers located in proximity to end-user consumption points for different uses, such as energy storage for fuel cells connected to the grid or power-to-gas. Concerning medium terms, large-scale green hydrogen generation can be a commercially viable solution with electrolyzers installed at the end-user site and powered by photovoltaic plants.

Funding: This research received no external funding.

Acknowledgments: The author would like to thank technician Giampiero Rizzo for the support in setting up the computational system and technician Giovanni Ruggieri for arranging the hardware to carry out the simulations given in this paper.

Author Contributions: All authors have read and agreed to the published version of the manuscript.

Conflicts of Interest: The author declares no conflicts of interest.

Appendix A. Maximum Efficiency Calculation

The dissipated power P_{diss} can be expressed as a function of the output power P_{o0} as in Equation (6), repeated here for convenience:

$$P_{diss} = k_o + k_l P_o + k_q P_o^2 \tag{A1}$$

The total efficiency is given by:

$$\eta = \frac{P_o}{P_o + P_{diss}} = \frac{1}{1 + \left(\frac{k_0}{P_0}\right) + k_l + k_q \cdot P_o} \tag{A2}$$

Since usually $P_{diss} << P_0$

$$\eta \approx 1 - \left[\left(\frac{k_0}{P_0}\right) + k_l + k_q \cdot P_o\right] \tag{A3}$$

The maximum efficiency is retrieved when:

$$\left(\frac{k_0}{P_0}\right) + k_l + k_q \cdot P_o \Rightarrow min \tag{A4}$$

it corresponds to the condition:

$$\left(\frac{k_0}{P_0}\right) = k_q \cdot P_o \tag{A5}$$

The maximum efficiency is:

$$\eta_{max} = 1 - k_l - 2\sqrt{k_0 \cdot k_q} \tag{A6}$$

and occurs at a power:

$$P_{0(\eta_{max})} = \sqrt{\frac{k_o}{k_2}} \tag{A7}$$

This last value usually differs from the rated power; for this reason, the efficiency in correspondence of the rated power is lower compared to the maximum.

As a final remark, the maximum power at which the maximum efficiency is obtained does not depend on k_l; however, it affects the maximum efficiency.

Appendix B. Analysis of the Main Losses in a Practical Case

A practical case study is proposed to show how losses in the main converter components affect efficiency. With reference to Figure 4, the photovoltaic source exploits a 156 × 156 mm Polycrystalline Silicon Cell by Risen Solar Technology [133]. The main parameters are summarized in Table A1. The field is formed by arrays containing 16 series-connected cells; four sets of two parallel-connected arrays are arranged to obtain the photovoltaic source.

The adopted electrolyzer is a PEM system, type NMH2-1000, by HELIOCENTRIS®. It is devised for educational purposes; the manufacturers provide a dedicated converter but here only the stack of the PEM electrolyzer is considered [134]. The main parameters are summarized in Table A2.

According to Figure 3, the electrolyzer has been modeled with R_{int} = 76 mΩ and V_{act} = 4.2 V.

The DC/DC stage is a buck converter as described in Section 5.1; it has been analyzed with real power devices whose parameters are given in Table A3. The switching frequency is set to 20 kHz. The analysis is carried out varying the input power supplied to the converter from 50 W to 550 W (obtained with solar radiation ranging from 100 W/m² to 1000 W/m²), and considering the conduction and the switching losses in the MOSFET (using Equations (9) and (10), respectively), conduction losses and the reverse recovery losses in the free-wheel diode (using Equations (8) and (11)) and Joule losses in the inductor (using Equation (12)). The losses are illustrated in Figure A1 (dynamic losses) and Figure A2 (static losses); two separate plots are drawn due to the different ordinate scales. Figure A1 shows the switching losses in the MOSFET and the reverse recovery losses in the free-wheel diode; the switching losses in the MOSFET are reduced thanks to the low values of the turn-on and turn-off time (see Equation (10)) equal to 5 ns for the device considered. Figure A2 shows the conduction losses in the MOSFET, the conduction losses in the free-wheel diode and the Joule losses in the inductor. It can be noted that the conduction losses in the free-wheel diode are linear, whereas both conduction losses in the MOSFET and the Joule losses in the inductor are quadratic, as expected. In addition, they are coincident due to the similar values of the conduction resistance of the MOSFET and of the parasitic resistance of the inductor. As a general remark, it can be noted that dynamic losses are reduced compared to conduction losses thanks to the fast-switching features of the devices considered.

Table A1. Characteristic parameters of the solar cell (measured under STC standard test conditions 1000 W/m², AM 1.5, 25 °C).

Parameter	Value	Unit

Pmpp	4.33	W
Vmpp	0.53	V
Impp	8.17	A
Voc	0.635	V
Isc	8.693	A
FF	78.44	%

Table A2. Characteristic parameters of the NMH2-1000 PEM electrolyzer.

Parameter	Value	Unit
Rated electric power	400	W
Stack voltage operating range	4.2–8	V
Stack current range	0–50	A
Operating temperature range	288.15–313.15	K
Hydrogen outlet pressure	10.5	Bar
Cells number	3	-
Active area section	50	cm^2
Hydrogen flow rate at STP (Standard Temperature and Pressure: 20 °C, 1 bar)	0–1	SLPM (Standard L/min)

Table A3. Main parameters of components adopted for the DC/DC buck converter.

Symbol	Rated Value	Supplier	Code
L	I_L = 10 A, L = 500 µH, R_L = 100 mΩ	Vishay-(Selb Germany)	IHV15BZ500
C	560 µF, Resr = 160 mΩ	Epcos (Milan Italy)	B43511A 4567M007
MOSFET	V_{DSS} = 650 V, R_{DS}(on) = 110 mΩ@25 °C; I_{DS} = 25 A	Infineon Techn. (Milan Italy)	IPA60R125CP CoolMOS

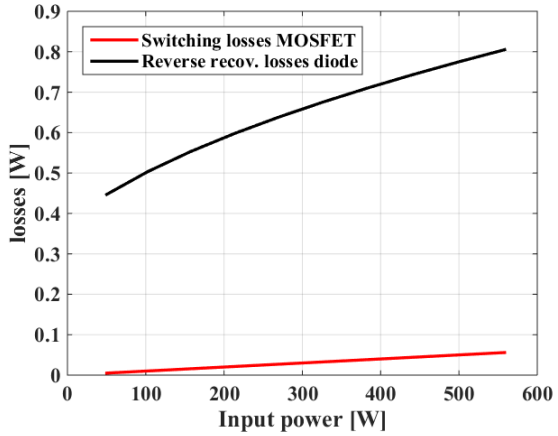

Figure A1. Switching losses in the MOSFET and reverse recovery losses in the free-wheel diode.

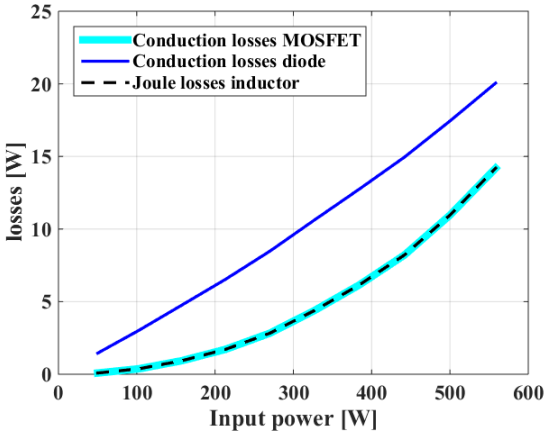

Figure A2. Conduction losses in the MOSFET, conduction losses in the free-wheel diode and Joule losses in the inductor.

A synoptic comparison of losses is provided in Figure A3 by a bar diagram, which encompasses the losses calculated at one-half of the rated power and at the rated power. It can be observed that the switching losses in the MOSFET and the reverse recovery losses in the diode remain negligible. Conduction losses are more significant. Particularly, the bar diagram highlights the quadratic behavior of both conduction losses in the diode and in the inductor, which, doubling the power, are quadrupled.

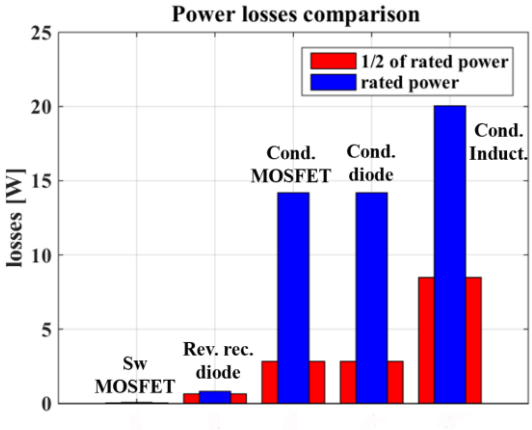

Figure A3. Synoptic comparison of losses, calculated at one half of the rated power and at the rated power.

Appendix C. Comparison of Efficiency Curves Between a Buck Converter and an Interleaved Configuration

The buck converter analyzed in Appendix B is now studied in an interleaved configuration, as described in Section 5.2, to compare the efficiency varying the number of legs from one to six. The efficiency curves are plotted in Figure A4. It can be noted that for higher power, increasing the number of operated legs improves efficiency because the current is shared among several devices so that quadratic losses are lessened; on the other hand, for low values of input power, reducing the number of operated legs is advantageous.

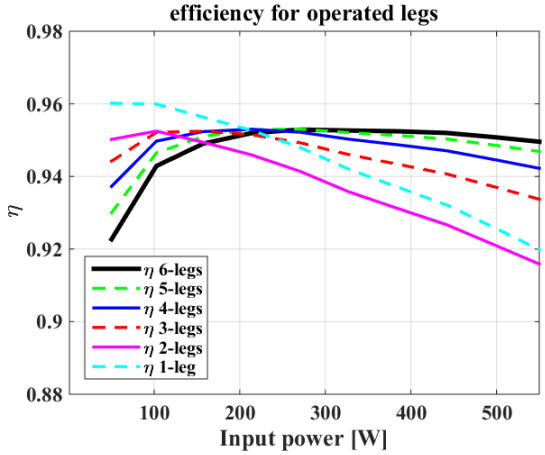

Figure A4. Efficiency curves of an interleaved buck converter varying the number of operated legs.

References

1. Pan, G.; Gu, Z.; Luo, E.; Gu, W. Analysis and Prospect of Electrolytic Hydrogen Technology Under Background of New Power Systems. *Autom. Electr. Power Syst*. **2023**, *47*, 1–13.
2. Yue, M.; Lambert, H.; Pahon, E.; Roche, R.; Jemei, S.; Hissel, D. Hydrogen energy systems: A critical review of technologies, applications, trends and challenges. *Renew. Sustain. Energy Rev*. **2021**, *146*, 111180.
3. Guilbert, D.; Vitale, G. Hydrogen as a clean and sustainable energy vector for global transition from fossil-based to zero-carbon. *Clean Technol.* **2021**, *3*, 881–909.
4. IRENA. *Green Hydrogen Cost Reduction: Scaling Up Electrolysers to Meet the 1.5 C° Climate Goal*; International Renewable Energy Agency: Abu Dhabi, UAE, 2020. Available online: https://www.irena.org/-/media/Files/IRENA/Agency/Publication/2020/Dec/IRENA_Green_hydrogen_cost_2020.pdf (accessed: 19th of November 2024).
5. Rogelj, J.; Shindell, D.; Jiang, K.; Fifita, S.; Forster, P.; Ginzburg, V.; Handa, C.; Kheshgi, H.; Kobayashi, S.; Kriegler, E.; et al. Mitigation pathways compatible with 1.5 C in the context of sustainable development. In *Global Warming of 1.5*; Intergovernmental Panel on Climate Change: Geneva, Switzerland, 2018; pp. 93–174. Available online: https://www.ipcc.ch/site/assets/uploads/sites/2/2019/02/SR15_Chapter2_Low_Res.pdf. pdf (accessed: 19th of November 2024).
6. 2030 Climate Targets. Available online: https://climate.ec.europa.eu/eu-action/climate-strategies-targets/2030-climate-targets_en#:~:text=In%202023%2C%20the%20EU%20adopted, climate%2Dneutral%20continent%20by%202050. pdf (accessed: 19th of November 2024)..
7. Lei, J.; Ma, H.; Qin, G.; Guo, Z.; Xia, P.; Hao, C. A Comprehensive Review on the Power Supply System of Hydrogen Production Electrolyzers for Future Integrated Energy Systems. *Energies* **2024**, *17*, 935.
8. Edwards, P.P.; Kuznetsov, V.; David, W.I. Hydrogen energy. *Philos. Trans. R. Soc. A Math. Phys. Eng. Sci.* **2007**, *365*, 1043–1056.
9. Nikolaidis, P.; Poullikkas, A. A comparative overview of hydrogen production processes. *Renew. Sustain. Energy Rev.* **2017**, *67*, 597–611.
10. Renaudineau, H.; Llor, A.M.; Cortés, R.; Rojas, C.A.; Restrepo, C.; Kouro, S. Photovoltaic green hydrogen challenges and opportunities: A power electronics perspective. *IEEE Ind. Electron. Mag.* **2021**, *16*, 31–41.
11. Xu, S.; Yu, B. Current development and prospect of hydrogen energy technology in China. *J. Beijing Inst. Technol.* **2021**, *23*, 1–12.
12. Abdelkareem, M.A.; Abdelghafar, A.A.; Mahmoud, M.; Sayed, E.T.; Mahmoud, M.S.; Alami, A.H.; Olabi, A.G. Optimized solar photovoltaic-powered green hydrogen: Current status, recent advancements, and barriers. *Sol. Energy* **2023**, *265*, 112072. https://doi.org/10.1016/j.solener.2023.112072.
13. Chi, J.; Yu, H. Water electrolysis based on renewable energy for hydrogen production. *Chin. J. Catal.* **2018**, *39*, 390–394. https://doi.org/10.1016/S1872-2067(17)62949-8.
14. Grube, T.; Reul, J.; Reuß, M.; Calnan, S.; Monnerie, N.; Schlatmann, R.; Sattler, C.; Robinius, M.; Stolten, D. A techno-economic perspective on solar-to-hydrogen concepts through 2025. *Sustain. Energy Fuels* **2020**, *4*, 5818–5834.
15. Mallapragada, D.S.; Gencer, E.; Insinger, P.; Keith, D.W.; O'Sullivan, F.M. Can industrial-scale solar hydrogen supplied from commodity technologies be cost competitive by 2030? *Cell Rep. Phys. Sci.* **2020**, *1*, 100174.
16. Longden, T.; Jotzo, F.; Prasad, M.; Andrews, R. *Green Hydrogen Production Costs in Australia: Implications of Renewable Energy and Electrolyser Costs*; CCEP: Canberra, ACT, Australia, 2020. Available online: https://iceds.anu.edu.au/files/2020%2009%2001%20-%20ZCEAP%20-%20CCEP%20Working%20Paper%20-%20Green%20hydrogen%20production%20costs.pdf (accessed: 19th November 2024).
17. Nicita, A.; Maggio, G.; Andaloro, A.; Squadrito, G. Green hydrogen as feedstock: Financial analysis of a photovoltaic powered electrolysis plant. *Int. J. Hydrogen Energy* **2020**, *45*, 11395–11408.

18. Bhattacharyya, R.; Misra, A.; Sandeep, K. Photovoltaic solar energy conversion for hydrogen production by alkaline water electrolysis: Conceptual design and analysis. *Energy Convers. Manag.* **2017**, *133*, 1–13.
19. Schmidt, O.; Gambhir, A.; Staffell, I.; Hawkes, A.; Nelson, J.; Few, S. Future cost and performance of water electrolysis: An expert elicitation study. *Int. J. Hydrogen Energy* **2017**, *42*, 30470–30492.
20. Guo, X.; Zhu, H.; Zhang, S. Overview of electrolyser and hydrogen production power supply from industrial perspective. *Int. J. Hydrogen Energy* **2023**, *49*, 1048–1059.
21. Sapountzi, F.M.; Gracia, J.M.; Weststrate, C.J.; Fredriksson, H.O.; Niemantsverdriet, J.H. Electrocatalysts for the generation of hydrogen, oxygen and synthesis gas. *Prog. Energy Combust. Sci.* **2017**, *58*, 1–35.
22. Guilbert, D.; Vitale, G. Dynamic emulation of a PEM electrolyzer by time constant based exponential model. *Energies* **2019**, *12*, 750.
23. Carmo, M.; Fritz, D.L.; Mergel, J.; Stolten, D. A comprehensive review on PEM water electrolysis. *Int. J. Hydrogen Energy* **2013**, *38*, 4901–4934.
24. Kumar, S.S.; Himabindu, V. Hydrogen production by PEM water electrolysis–a review. *Mater. Sci. Energy Technol.* **2019**, *2*, 442–454.Razi, F.; Dincer, I. A critical evaluation of potential routes of solar hydrogen production for sustainable development. *J. Clean. Prod.* **2020**, *264*, 121582.
26. De Lorenzo, G.; Agostino, R.G.; Fragiacomo, P. Dynamic electric simulation model of a proton exchange membrane electrolyzer system for hydrogen production. *Energies* **2022**, *15*, 6437.
27. Ouabi, H.; Lajouad, R.; Kissaoui, M.; El Magri, A. Hydrogen production by water electrolysis driven by a photovoltaic source: A review. *e-Prime-Adv. Electr. Eng. Electron. Energy* **2024**, *8*, 100608.
28. Yu, H.; Shao, Z.; Hou, M.; Yi, B.; Duan, F.; Yang, Y. Hydrogen Production by Water Electrolysis: Progress and Suggestions. *Chin. J. Eng. Sci*. **2021**, *23*, 146–152.
29. Łosiewicz, B. Recent Advances in Technologies of Green Hydrogen Production. *Energies* **2024**, *17*, 4514.
30. Xu, S. Current Development and Prospect of Hydrogen Energy Technology in China. J. *Beijing Inst. Technol.* **2021**, *23*, 1–12.
31. Lei, J.; Ma, H.; Qin, G.; Guo, Z.; Xia, P.; Hao, C. A Comprehensive Review on the Power Supply System of Hydrogen Production Electrolyzers for Future Integrated Energy Systems. *Energies* **2024**, *17*, 935.
32. Abdin, Z.; Zafaranloo, A.; Rafiee, A.; Mérida, W.; Lipiński, W.; Khalilpour, K.R. Hydrogen as an energy vector. *Renew. Sustain. Energy Rev.* **2020**, *120*, 109620.
33. Ursua, A.; Gandia, L.M.; Sanchis, P. Hydrogen production from water electrolysis: Current status and future trends. *Proc. IEEE* **2011**, *100*, 410–426.
34. Ishaq, H.; Dincer, I. Comparative assessment of renewable energy-based hydrogen production methods. *Renew. Sustain. Energy Rev.* **2021**, *135*, 110192.
35. Barbir, F.; PEM electrolysis for production of hydrogen from renewable energy sources. *Sol. Energy* **2005**, *78*, 661–669.
36. Nguyen, B.L.; Panwar, M.; Hovsapian, R.; Nagasawa, K.; Vu, T.V. Power converter topologies for electrolyzer applications to enable electric grid services. In Proceedings of the IECON 2021–47th Annual Conference of the IEEE Industrial Electronics Society, Sheraton Centre, Toronto, ON, Canada, 13–16 October 2021.
37. Andrijanovitsh, A.; Steiks, I.; Zakis, J.; Vinnikov, D. Analysis of state-of-the-art converter topologies for interfacing of hydrogen buffer with renewable energy systems. *Electr. Control Commun. Eng.* **2011**, *29*, 87–94.
38. Koponen, J.; Poluektov, A.; Ruuskanen, V.; Kosonen, A.; Niemelä, M.; Ahola, J. Comparison of thyristor and insulated-gate bipolar transistor-based power supply topologies in industrial water electrolysis applications. *J. Power Sources* **2021**, *491*, 229443.
39. Chen, M.; Chou, S.F.; Blaabjerg, F.; Davari, P. Overview of power electronic converter topologies enabling large-scale hydrogen production via water electrolysis. *Appl. Sci.* **2022**, *12*, 1906.
40. Koundi, M.; El Fadil, H.; EL Idrissi, Z.; Lassioui, A.; Intidam, A.; Bouanou, T.; Nady, S.; Rachid, A. Investigation of Hydrogen Production System-Based PEM EL: PEM EL Modeling, DC/DC Power Converter, and Controller Design Approaches. *Clean Technol.* **2023**, *5*, 531–568. https://doi.org/10.3390/cleantechnol5020028.
41. Guilbert, D.; Collura, S.M.; Scipioni, A. DC/DC converter topologies for electrolyzers: State-of-the-art and remaining key issues. *Int. J. Hydrogen Energy* **2017**, *42*, 23966–23985.
42. Guida, V.; Guilbert, D.; Douine, B. Candidate interleaved dc-dc buck converters for electrolyzers: State-of-the-art and perspectives. In Proceedings of the 2018 IEEE International Conference on Environment and Electrical Engineering and 2018 IEEE Industrial and Commercial Power Systems Europe (EEEIC/I&CPS Europe), Palermo, Italy, 12–15 June 2018.
43. Guida, V.; Guilbert, D.; Douine, B. Literature survey of interleaved dc-dc step-down converters for proton exchange membrane electrolyzer applications. *Trans. Environ. Electr. Eng.* **2019**, *3*, 33–43.
44. Yodwong, B.; Guilbert, D.; Phattanasak, M.; Kaewmanee, W.; Hinaje, M.; Vitale, G. AC-DC converters for electrolyzer applications: State of the art and future challenges. *Electronics* **2020**, *9*, 912.
45. Zorica, S.; Vukšić, M.; Betti, T. Design considerations of the multi-resonant converter as a constant current source for electrolyser utilisation. *Int. J. Electr. Power Energy Syst.* **2019**, *111*, 237–247.
46. Kandah, M.I. Enhancement of water electrolyzer efficiency. *J. Energy Technol. Policy* **2014**, *4*, 1–9.
47. Ngoh, K.S.; Njomo, D. An overview of hydrogen gas production from solar energy. *Renew. Sustain. Energy Rev.* **2012**, *16*, 6782–6792.
48. Grimes, C.A.; Oomman, K.V.; Ranjan, S. Hydrogen Generation by Water Splitting. In *Light, Water, Hydrogen: The Solar Generation of Hydrogen by Water Photoelectrolysis*; Springer: Berlin/Heidelberg, Germany, 2008; pp.35–51.

49. Bovo, A.; Poli, N.; Trovò, A.; Marini, G.; Guarnieri, M. Hydrogen energy storage system in a multi–technology microgrid: Technical features and performance. *Int. J. Hydrogen Energy* **2023**, *48*, 12072–12088.
50. Parache, F.; Schneider, H.; Turpin, C.; Richet, N.; Debellemanière, O.; Bru, É.; Thieu, A.T.; Bertail, C.; Marot, C. Impact of Power Converter Current Ripple on the Degradation of PEM Electrolyzer Performances. *Membranes* **2022**, *12*, 109. https://doi.org/10.3390/membranes12020109.
51. Erickson, R.W.; Maksimović, D. Input Filter Design. In *Fundamentals of Power Electronics,* 3rd ed.; CRC Press: Boca Raton, FL, USA, 2020; pp. 675–721.
52. Guilbert, D.; Sorbera, D.; Vitale, G. A stacked interleaved dc-dc buck converter for proton exchange membrane electrolyzer applications: Design and experimental validation. *Int. J. Hydrogen Energy* **2020**, *45*, 64–79.
53. Kolar, J.W.; Krismer, F.; Lobsiger, Y.; Muhlethaler, J.; Nussbaumer, T.; Minibock, J. Extreme efficiency power electronics. In Proceedings of the 7th International Conference on Integrated Power Electronics Systems (CIPS), Nuremberg, Germany, 6–8 March 2012.
54. Application Manual Power Semiconductors. Available online: https://www.semikron-danfoss.com/service-support/application-manual.html. (accessed: 19th November 2024).
55. Haaf, P.; Harper, J. Understanding diode reverse recovery and its effect on switching losses. In *Fairchild Power Seminar*; Fairchild: Sunnyvale, CA, USA, 2007; Volume 2007. Available online: https://www.mikrocontroller.net/attachment/351267/Understanding-Diode-Reverse-Recovery-and-Its-Effect-on-Switching-Losses.pdf (accessed: 19th November 2024).
56. Amaral, A.M.R.; Cardoso, A.J.M. On-line fault detection of aluminium electrolytic capacitors, in step-down DC–DC converters, using input current and output voltage ripple. *IET Power Electron.* **2012**, *5*, 315–322.
57. Wang, H.; Blaabjerg, F.; Reliability of capacitors for DC-link applications in power electronic converters—An overview. *IEEE Trans. Ind. Appl.* **2014**, *50*, 3569–3578.
58. Svensson, L. Adiabatic and Clock-Powered Circuits. In *Low-Power Electronics Design*; Piguet, L., Ed.; CRC Press: Boca Raton, FL, USA, 2004; pp. 240–254.
59. Piazza, M.C.; Ragusa, A.; Vitale, G. Power-loss evaluation in CM active EMI filters for bearing current suppression. *IEEE Trans. Ind. Electron.* **2011**, *58*, 5142–5153.
60. Boglietti, A.; Cavagnino, A.; Lazzari, M.; Pastorelli, M. Predicting iron losses in soft magnetic materials with arbitrary voltage supply: An Engineering Approach. *IEEE Trans. Magn*. **2003**, *39*, 981–989.
61. Moses, A.J. Power loss of non oriented electrical steel under square wave excitation. *IEEE Trans. Magn.* **2001**, *37*, 2737–2739.
62. Abramovitz, A.; Ben Yaakov, S. RGSE-Based SPICE Modelling of Ferrite Core Losses. *IEEE Trans. on Power Electr*. **2017**, *33*, 2825–2831.
63. Roberto, S.F.; Sciré, D.; Lullo, G.; Vitale, G. Equivalent circuit modelling of ferrite inductors losses. In Proceedings of the 4th International Forum on Research and Technology for Society and Industry (RTSI), Palermo, Italy, 10–13 September 2018.
64. Vitale, G.; Lullo, G.; Scirè, D. Thermal stability of a DC/DC converter with inductor in partial saturation. *IEEE Trans. Ind. Electron.* **2020**, *68*, 7985–7995.
65. Ahmad, G.E.; El Shenawy, E.T. Optimized photovoltaic system for hydrogen production. *Renew. Energy* **2006**, *31*, 1043–1054.
66. Gibson, T.L.; Kelly, N.A. Predicting efficiency of solar powered hydrogen generation using photovoltaic-electrolysis devices. *Int. J. Hydrogen Energy* **2010**, *35*, 900–911.
67. Gibson, T.L.; Kelly, N.A. Optimization of solar powered hydrogen production using photovoltaic electrolysis devices. *Int. J. Hydrogen Energy* **2008**, *33*, 5931–5940.
68. Mao, S.; Wu, T.; Lu, X.; Popovic, J.; Ferreira, J.A. Three-phase active front-end rectifier efficiency improvement with silicon carbide power semiconductor devices. In Proceeding of the 2016 IEEE Energy Conversion Congress and Exposition (ECCE), Milwaukee, WI, USA, 18–22 September 2016.
69. Sánchez, L.; Reigosa, D.; Bilbao, A.; Peña-Gonzalez, I.; Briz, F. Comparative Analysis of Power Converter Topologies for Hydrogen Electrolyzers. *IEEE J. Emerg. Sel. Top. Power Electron.* **2024**, *12*, 4325–4341.
70. Dahbi, S.; Aboutni, R.; Aziz, A.; Benazzi, N.; Elhafyani, M.; Kassmi, K. Optimised hydrogen production by a photovoltaic-electrolysis system DC/DC converter and water flow controller. *Int. J. Hydrogen Energy* **2016**, *41*, 20858–20866.
71. Şahin, M.E. A photovoltaic powered electrolysis converter system with maximum power point tracking control. *Int. J. Hydrogen Energy* **2020**, *45*, 9293–9304.
72. Guilbert, D.; Yodwong, B.; Kaewmanee, W.; Phattanasak, M.; Hinaje, M. Hydrogen Flow Rate Control of a Proton Exchange Membrane Electrolyzer. In Proceedings of the 2019 Research, Invention, and Innovation Congress (RI2C), Bangkok, Thailand, 11–13 December 2019.
73. Sahin, M.E.; Okumus, H.I.; Aydemir, M.T. Implementation of an electrolysis system with dc/dc synchronous buck converter. *Int. J. Hydrogen Energy* **2014**, *39*, 6802–6812.
74. Pipitone, E.; Vitale, G. A regenerative braking system for internal combustion engine vehicles using supercapacitors as energy storage elements-Part 1: System analysis and modeling. *J. Power Sources* **2020**, *448*, 227368.
75. Sferlazza, A.; Garraffa, G.; Vitale, G.; D'Ippolito, F.; Alonge, F.; Lullo, G.; Busacca, A.; Giaconia, G.C.; Scirè, D. Robust Disturbance Rejection Control of DC/DC Interleaved Boost Converters with Additional Sliding Mode Component. In Proceedings of the 2023 Asia Meeting on Environment and Electrical Engineering (EEE-AM) Hanoi, Vietnam, 13–15 November 2023.

76. Yao, K.; Qiu, Y.; Xu, M.; Lee, F.C. A novel winding-coupled buck converter for high-frequency, high-step-down DC-DC conversion, *IEEE Trans. Power Electron.* **2005**, *20*, 1017–1024.
77. Ilic, M.; Maksimovic, D. Interleaved Zero-Current-Transition Buck Converter. *IEEE Trans. Ind. Appl.* **2007**, *43*, 1619–1627.
78. Zhang, H.; Lu, Y.; Zhang, J.; Benigni, A. Real-time simulation of an electrolyzer with a diode rectifier and a threephase interleaved buck converter. In Proceedings of the 2022 IEEE 13th International Symposium on Power Electronics for Distributed Generation Systems (PEDG), Kiel, Germany 26–29 June 2022.
79. Pellitteri, F.; Campagna, N.; Inguanta, R.; Miceli, R. Application of a multiphase interleaved DC-DC converter for power-to-hydrogen systems. In Proceedings of the 17th International Conference on Compatibility, Power Electronics and Power Engineering (CPE-POWERENG), Tallinn, Estonia, 14–16 June 2023.
80. Yodwong, B.; Sikkabut, S.; Guilbert, D.; Hinaje, M.; Phattanasak, M.; Kaewmanee, W.; Vitale, G. Open-circuit switch fault diagnosis and accommodation of a three-level interleaved buck converter for electrolyzer applications. *Electronics* **2023**, *12*, 1349.
81. Yodwong, B.; Guilbert, D.; Kaewmanee, W.; Phattanasak, M.; Hinaje, M.; Vitale, G. Improved Sliding Mode-Based Controller of a High Voltage Ratio DC–DC Converter for Electrolyzers Supplied by Renewable Energy. *IEEE Trans. Ind. Electron.* **2023**, *71*, 8831–8840.
82. Jørgensen, K.L.; Zhang, Z.; Andersen, M.A. Next generation of power electronic-converter application for energy conversion and storage units and systems. *Clean Energy* **2019**, *3*, 307–315.
83. Mira, M.C.; Zhang, Z.; Jørgensen, K.L.; Andersen, M.A. Fractional charging converter with high efficiency and low cost for electrochemical energy storage devices. *IEEE Trans. Ind. Appl.* **2019**, *55*, 7461–7470.
84. Anzola, J.; Aizpuru, I.; Romero, A.A.; Loiti, A.A.; Lopez-Erauskin, R.; Artal-Sevil, J.S.; Bernal, C. Review of architectures based on partial power processing for dc-dc applications. *IEEE Access* **2020**, *8*, 103405–103418.
85. Duc, T.N.; Goshome, K.; Endo, N.; Maeda, T. Optimization strategy for high efficiency 20 kW-class direct coupled photovoltaic-electrolyzer system based on experiment data. *Int. J. Hydrogen Energy* **2019**, *44*, 26741–26752.
86. Clarke, R.; Giddey, S.; Ciacchi, F.; Badwal, S.; Paul, B.; Andrews, J. Direct coupling of an electrolyser to a solar PV system for generating hydrogen. *Int. J. Hydrogen Energy* **2009**, *34*, 2531–2542.
87. Mraoui, A.; Benyoucef, B.; Hassaine, L. Experiment and simulation of electrolytic hydrogen production: Case study of photovoltaic-electrolyzer direct connection. *Int. J. Hydrogen Energy* **2018**, *43*, 3441–3450.
88. Gaamouche, R.; Abbou, A.; Redouane, A.; El Hasnaoui, A.; Belhorma, B. Modeling and simulation of direct coupling of an electrolyzer to PV system for hydrogen production. In Proceedings of the 2018 6th IEEE International Renewable and Sustainable Energy Conference (IRSEC), Rabat, Morocco, 5–8 December 2018.
89. X.] Acar, C.; Erturk, E.; Firtina-Ertis, I. Performance analysis of a stand-alone integrated solar hydrogen energy system for zero energy buildings. *Int. J. Hydrogen Energy* **2023**, *48*, 1664–1684.
90. Arriaga, L.G.; Martinez, W.; Cano, U.; Blud, H. Direct coupling of a solar-hydrogen system in Mexico. *Int. J. Hydrogen Energy* **2007**, *32*, 2247–2252.
91. Khalilnejad, A.; Sundararajan, A.; Sarwat, A.I. Performance evaluation of optimal photovoltaic-electrolyzer system with the pur-pose of maximum hydrogen storage. In Proceedings of the 2016 IEEE/IAS 52nd Industrial and Commercial Power Systems Technical Conference (I&CPS) Detroit, MI, USA, 1–5 May 2016.
92. Cai, X.; Lin, R.; Xu, J.; Lu, Y. Construction and analysis of photovoltaic directly coupled conditions in PEM electrolyzer. *Int. J. Hydrogen Energy* **2022**, *47*, 6494–6507.
93. Di Caro, A.; Vitale, G. Direct-Coupled Improvement of a Solar-Powered Proton Exchange Membrane Electrolyzer by a Reconfigurable Source. *Clean Technol.* **2024**, *6*, 1203–1228.
94. Van, L.P.; Hoang, L.H.; Duc, T.N. A comprehensive review of direct coupled photovoltaic-electrolyser system: Sizing techniques, operating strategies, research progress, current challenges, and future recommendations. *Int. J. Hydrogen Energy* **2023**, *48*, 25231–25249.
95. Andrijanovitsh, A.; Steiks, I.; Zakis, J.; Vinnikov, D. Analysis of state-of-the-art converter topologies for interfacing of hydrogen buffer with renewable energy systems. *Electr. Control Commun. Eng.* **2011**, *29*, 87–94.
96. Gautam, D.S.; Bhat, A.K. A comparison of soft-switched DC-to-DC converters for electrolyzer application. *IEEE Trans. Power Electron.* **2012**, *28*, 54–63.
97. Sabate, J.; Vlatkovic, V.; Ridley, R. Design considerations for high-voltage high-power full-bridge zero-voltage swltclled pwm converter. In Proceedings of the Fifth Annual Proceedings on Applied Power Electronics Conference and Exposition IEEE APEC, Los Angeles, CA, USA, 11–16 March 1990.
98. Chandrasekhar, P.; Rama Reddy, S. Design of LLC resonant converter for electrolyser. **2011**, *International Journal on Electrical Engineering and Informatics - Vol. 3, N. 3.*
99. Garrigós, A.; Blanes, J.M.; Carrasco, J.A.; Lizán, J.L.; Beneito, R.; Molina, J.A. 5 kW DC/DC converter for hydrogen generation from photovoltaic sources. *Int. J. Hydrogen Energy* **2010**, *35*, 6123–6130.
100. Erich, S.Y.; Polivka, W.A. Input filter design criteria for current-programmed regulators. *IEEE Trans. Power Electron.* **1992**, *7*, 143–151.
101. Garrigós, A.; Lizán, J.L.; Blanes, J.M.; Gutiérrez, R. Combined maximum power point tracking and output current control for a photovoltaic-electrolyser DC/DC converter. *Int. J. Hydrogen Energy* **2014**, *39*, 20907–20919.
102. Blinov, A.; Andrijanovits, A. New DC/DC converter for electrolyser interfacing with stand-alone renewable energy system. *Electr. Control Commun. Eng.* **2012**, *1*, 24–29.

103. Sun, J.; Webb, K.F.; Mehrotra, V. An improved current-doubler rectifier with integrated magnetics. In Proceedings of the Seventeenth Annual IEEE Applied Power Electronics Conference and Exposition APEC, Dallas, TX, USA, 10–14 March 2002.
104. Andrijanovitš, A.; Vinnikov, D.; Roasto, I.; Blinov, A. Three-level half-bridge ZVS DC/DC converter for electrolyzer integration with renewable energy systems. In Proceedings of the 10th International Conference on Environment and Electrical Engineering, Rome, Italy, 8–11 May 2011.
105. Balogh, L. *The Current-Doubler Rectifier: An Alternative Rectification Technique for Push-Pull and Bridge Converters*; Unitrode: Manchester, NH, USA, 1994; 3p. Available online: https://www.ti.com/lit/an/slua121/slua121.pdf?ts=1724676914976&ref_url=https%253A%252F%252Fwww.google.com%252F (accessed: 19th November 2024).
106. Vukšić, M.; Beroš, S.M.; Vukšić, L. The multiresonant converter steady-state analysis based on dominant resonant process. *IEEE Trans. Power Electron.* **2011**, *26*, 1452–1468.
107. Cavallaro, C.; Cecconi, V.; Chimento, F.; Musumeci, S.; Santonocito, C.; Sapuppo, C. A phase-shift full bridge converter for the energy management of electrolyzer systems. In proceedings of 2007 IEEE International Symposium on Industrial Electronics, Vigo, Spain, 4–7 June 2007; pp. 2649–2654.
108. Gautam, D.S.; Bhat, A.K. A comparison of soft-switched DC-to-DC converters for electrolyzer application. *IEEE Trans. Power Electron.* **2012**, *28*, 54–63.
109. Bodur, H.; Bakan, A.F. A new ZVT-PWM dc-dc converter. *IEEE Trans. Power Electron.* **2002**, *17*, 40–47.
110. Ting, N.S.; Sahin, Y.; Aksoy, I. A new ZVT-PWM interleaved dc-dc boost converter. In Proceedings of the 2015 Intl Aegean Conference on Electrical Machines & Power Electronics (ACEMP), 2015 Intl Conference on Optimization of Electrical & Electronic Equipment (OPTIM) & 2015 Intl Symposium on Advanced Electromechanical Motion Systems (ELECTROMOTION), Side, Turkey, 2–4 September 2015.
111. Concha, D.; Renaudineau, H.; Hernandez, M.S.; Llor, A.M.; Kouro, S. Evaluation of DCX converters for off-grid photovoltaic-based green hydrogen production. *Int. J. Hydrogen Energy* **2021**, *46*, 19861–19870.
112. Wu, X.; Shi, H. High efficiency high density 1 MHz 380–12V DCX with low FOM devices. *IEEE Trans. Ind. Electron.* **2020**, *67*, 1648e56.
113. Neumayr, D.; Vohringer, M.; Chrysogelos, N.; Deboy, G.; Kolar, J.W. P3dctdpartial-power pre-regulated dc transformer. *IEEE Trans. Power Electron.* **2019**, *34*, 6036e47.
114. Vinnikov, D.; Andrijanovitš, A.; Roasto, I.; Jalakas, T. Experimental study of new integrated DC/DC converter for hydrogen-based energy storage. In Proceedings of the 2011 10th International Conference on Environment and Electrical Engineering, Rome, Italy, 8–11 May 2011.
115. Vinnikov, D.; Roasto, I. Quasi-Z-Source-Based Isolated DC/DC Converters for Distributed Power Generation. *IEEE Trans. Ind. Electron.* **2011,** *58*, 192–201.
116. Andrijanovitš, A.; Blinov, A.; Husev, O.; Vinnikov, D. Multiport converter with integrated energy storage for hydrogen buffer interfacing with renewable energy systems. In Proceedings of the 2012 IEEE International Conference on Industrial Technology, Athens, Greece, 19–21 March 2012.
117. Agbossou, K.; Doumbia, M.; Anouar, A. Optimal hydrogen production in a stand-alone renewable energy system. In Proceedings of the Fourtieth IAS Annual Meeting, Conference Record of the 2005 Industry Applications Conference, Hong Kong, China, 2–6 October 2005; Volume 4, pp. 2932–2936.
118. Zhou, J.; Meng, X.; Chen, Y.; Zhang, G. Research on DC Power Supply for Hydrogen Production from Electrolytic Water Based on New Energy Generation, *J. Phys. Conf. Ser.* **2023**, *2465*, 012007.
119. Jahdi, S.; Kumar, A.S.; Deakin, M.; Taylor, P.C.; Kuball, M. β-Ga2O3 in Power Electronics Converters: Opportunities & Challenges. *IEEE Open J. Power Electron.* **2024**, *5*, 554–564.
120. Buffolo, M.; Favero, D.; Marcuzzi, A.; De Santi, C.; Meneghesso, G.; Zanoni, E.; Meneghini, M. Review and outlook on GaN and SiC power devices: Industrial state-of-the-art, applications, and perspectives. *IEEE Trans. Electron Devices* **2024**, *71*, 1344–1355.
121. Wang, K.; Li, B.; Li, H.; Yang, X.; Qiu, A. Characterization and Modeling of Frequency-Dependent On-Resistance for GaN Devices at High Frequencies. *IEEE Trans. Power Electron*. **2020**, *35*, 4925–4933.
122. Sandler, S. Faster-Switching GaN: Presenting a number of interesting measurement challenges. *IEEE Power Electron. Mag.* **2015**, *2*, 24–31.
123. Azpurua, M.A.; Pous, M.; Silva, F. Time- and Frequency-Domain Characterization of Switching Losses in GaN FETs Power Converters. *IEEE Trans. Power Electron*. **2021**, *37*, 3219–3232.
124. Vella, A.; Galioto, G.; Vitale, G.; Lullo, G.; Giaconia, G.C. GaN and SiC Device Characterization by a Dedicated Embedded Measurement System. *Electronics* **2023**, *12*, 1555.
125. Wang, B.; Sun, L.; Diao, N.; Zhang, L.; Guo, X.; Guerrero, J.M. GaN-based step-down power converter and control strategy for hydrogen energy systems. *Energy Rep.* **2023**, *9*, 252–259.
126. Fritz, N.; Sechel, T.; Kowalewski, P.; De Doncker, R.W. Optimizing current-fed, GaN-based DC-DC converters for electrolysis applications. In proceedings of 11th International Conference on Power Electronics and ECCE Asia (ICPE 2023-ECCE Asia), Jeju, Korea, (22–25 May 2023).
127. Kavlak, G.; McNerney, J.; Trancik, J.E. Evaluating the causes of cost reduction in photovoltaic modules. *Energy Policy* **2018,** *123*, 700–710.

128. Jayachandran, M.; Gatla, R.K.; Flah, A.; Milyani, A.H.; Milyani, H.M.; Blazek, V.; Kraiem, H. Challenges and opportunities in green hydrogen adoption for decarbonizing hard-to-abate industries: A comprehensive review. *IEEE Access* **2024**, *12*, 23363–23388.
129. Hughes, J.P.; Clipsham, J.; Chavushoglu, H.; Rowley-Neale, S.J.; Banks, C.E. Polymer electrolyte electrolysis: A review of the activity and stability of non-precious metal hydrogen evolution reaction and oxygen evolution reaction catalysts. *Renew. Sustain. Energy Rev*. **2021**, 139, 110709.
130. International Renewable Energy Agency. *Innovation Trends in Electrolysers for Hydrogen Production*; International Renewable Energy Agency: Masdar City, UAE. 2022. Available online: https://www.irena.org/-/media/Files/IRENA/Agency/Publication/2022/May/IRENA_EPO_Electrolysers_H2_production_2022.pdf?rev=647d930910884e51b60137bcf5a955a6 (accessed: 19th November 2024).
131. Tashie-Lewis, B.C.; Nnabuife, S.G. Hydrogen production, distribution, storage and power conversion in a hydrogen economy—A technology review. *Chem. Eng. J. Adv.* **2021**, *8*, 100172.
132. Abohamzeh, E.; Salehi, F.; Sheikholeslami, M.; Abbassi, R.; Khan, F. Review of hydrogen safety during storage, transmission, and applications processes. *J. Loss Prev. Process Ind*. **2021**, *72*, 104569.
133. Poly 156*156mm. Available online: https://www.enfsolar.com/pv/cell-datasheet/919 (accessed: 19th November 2024).
134. Hydrogen Generator. Available online: https://www.heliocentrisacademia.com/hydrogen-generator/p1520?currency=usd (accessed: 19th November 2024).